

Journal of Geophysical Research: Atmospheres

RESEARCH ARTICLE

10.1002/2015JD024257

Key Points:

- Introduces an IVT-based AR detection algorithm suitable for global studies
- Evaluates performance of the algorithm relative to previous studies in three regions
- Investigates climatology/seasonality/variability of global AR characteristics using the algorithm

Correspondence to:

B. Guan,
bin.guan@jpl.nasa.gov

Citation:

Guan, B., and D. E. Waliser (2015), Detection of atmospheric rivers: Evaluation and application of an algorithm for global studies, *J. Geophys. Res. Atmos.*, 120, 12,514–12,535, doi:10.1002/2015JD024257.

Received 21 SEP 2015

Accepted 25 NOV 2015

Accepted article online 28 NOV 2015

Published online 28 DEC 2015

Detection of atmospheric rivers: Evaluation and application of an algorithm for global studies

Bin Guan^{1,2} and Duane E. Waliser^{1,2}¹Joint Institute for Regional Earth System Science and Engineering, University of California, Los Angeles, California, USA,²Jet Propulsion Laboratory, California Institute of Technology, Pasadena, California, USA

Abstract Atmospheric rivers (ARs) are narrow, elongated, synoptic jets of water vapor that play important roles in the global water cycle and regional weather/hydrology. A technique is developed for objective detection of ARs on the global domain based on characteristics of the integrated water vapor transport (IVT). AR detection involves thresholding 6-hourly fields of ERA-Interim IVT based on the 85th percentile specific to each season and grid cell and a fixed lower limit of $100 \text{ kg m}^{-1} \text{ s}^{-1}$ and checking for the geometry requirements of length $>2000 \text{ km}$, length/width ratio >2 , and other considerations indicative of AR conditions. Output of the detection includes the AR shape, axis, landfall location, and basic statistics of each detected AR. The performance of the technique is evaluated by comparison to AR detection in the western North America, Britain, and East Antarctica with three independently conducted studies using different techniques, with over ~90% agreement in AR dates. Among the parameters tested, AR detection shows the largest sensitivity to the length criterion in terms of changes in the resulting statistical distribution of AR intensity and geometry. Global distributions of key AR characteristics are examined, and the results highlight the global footprints of ARs and their potential importance on global and regional scales. Also examined are seasonal dependence of AR frequency and precipitation and their modulation by four prominent modes of large-scale climate variability. The results are in broad consistency with previous studies that focused on landfalling ARs in the west coasts of North America and Europe.

1. Introduction

Atmospheric rivers (ARs) are narrow, elongated, synoptic jets of water vapor that play important roles in the global water cycle and regional weather and hydrology. Based on 3 years of analysis data from the European Centre for Medium-Range Weather Forecasts (ECMWF), Zhu and Newell [1998] estimated that ARs, while covering ~10% of the Earth's circumference at midlatitudes, account for over 90% of the total poleward water vapor transport at these latitudes. A typical AR may carry as much water as 7–15 Mississippi Rivers [Ralph and Dettinger, 2011], and there are typically three to five ARs in each hemisphere at any given time [Zhu and Newell, 1998]. Enhanced precipitation may occur when the moisture-laden ARs hit major landmasses, penetrate inland, and interact with the topography. In the western U.S. and other water-stressed areas, ARs produce beneficial rain and snow that form a crucial source of fresh water [Guan et al., 2010; Dettinger et al., 2011; Rutz and Steenburgh, 2012] and can often break existing drought conditions [Dettinger, 2013]. On the other hand, extreme precipitation associated with ARs can lead to floods and related damages [Ralph et al., 2006; Leung and Qian, 2009; Neiman et al., 2011; Neiman et al., 2013]. A minireview of the basic characteristics of ARs can be found in Gimeno et al. [2014].

Previous studies have developed techniques for objective identification of ARs based on intensity and/or geometry thresholds indicative of AR conditions. Such techniques have facilitated the investigation of AR characteristics and impacts in several midlatitude regions. These techniques can roughly be categorized into three types. The simplest type of method is based on thresholding low-level wind and integrated water vapor (IWV) values at a single observation site or model grid cell without explicit consideration of the AR geometry [Neiman et al., 2009; Dettinger, 2011; Ralph et al., 2013]. This type of method is useful for studying AR landfalls in small, local areas and can best take advantage of high quality in situ observations from individual sites. The second type of method is based on the preselection of a certain cross section in the region of interest and tracking spatial features in a moisture-related field intersecting the cross section while satisfying a set of criteria for AR length/orientation and intensity [Lavers et al., 2011; Lavers et al., 2012; Nayak et al., 2014; Gao et al., 2015]. This type of method has facilitated regional studies where AR landfall is a focus, without the complexity of more sophisticated methods. The need to preselect a certain cross section makes it less desirable

for applications to larger/global domains where the interest is not limited to locations where ARs ultimately make landfalls. The third type of method takes full consideration of the AR morphology and involves the identification of long and narrow features characteristic of ARs at any location of a given domain, making it desirable for studies where the spatial distribution of ARs over a large domain is of interest. Several IWV-based algorithms have been developed using this method [Wick *et al.*, 2013; Jiang *et al.*, 2014; Hagos *et al.*, 2015] based on the earlier establishment of the IWV AR criteria to take advantage of satellite IWV observations [Ralph *et al.*, 2004; Neiman *et al.*, 2008].

Compared to IWV, the integrated water vapor transport (IVT) is a more desirable variable for AR detection due to its direct relationship with orographically induced precipitation [Neiman *et al.*, 2002; Neiman *et al.*, 2009] and its usefulness in understanding AR's role in the global water cycle [Zhu and Newell, 1998]. IVT-based AR detection techniques using the third type of method above have been developed for studying ARs affecting the western U.S. and facilitated the investigation of AR's characteristics during landfall and inland penetration [Rutz *et al.*, 2014; Backes *et al.*, 2015]. AR's global signatures [Waliser *et al.*, 2012], including those in less explored areas such as Greenland [Neff *et al.*, 2014] and Antarctica [Gorodetskaya *et al.*, 2014], and the need for understanding the representation of ARs in global weather/climate models motivate the development and evaluation of an AR detection technique suitable for global studies. The main objectives of the current study are to (1) introduce an IVT-based technique for global AR detection, (2) evaluate the performance of the technique relative to previous studies, and (3) examine global AR characteristics, including their seasonal dependence and climate modulation, based on the technique.

2. Data

2.1. IVT, IWV, and Precipitation

The primary data set used is the ECMWF Interim reanalysis (ERA-Interim) [Dee *et al.*, 2011], which provides global, 6-hourly atmospheric fields at $1.5^\circ \times 1.5^\circ$ spatial resolution. Key AR characteristics are well represented in ERA-Interim IVT based on comparison to aircraft observation of six ARs over the northeastern Pacific [Ralph *et al.*, 2012]. AR detection is based on IVT derived from specific humidity and wind fields at 17 pressure levels between 1000 and 300 hPa inclusive. The land-sea mask from the same data set is used for the detection of AR landfall. IWV derived from specific humidity is also used in the analysis. An additional reanalysis product, namely, the National Aeronautics and Space Administration (NASA) Modern-Era Retrospective Analysis for Research and Applications (MERRA) [Rienecker *et al.*, 2011], is used in the analysis of the sensitivity of AR detection to input data. For this, 6-hourly MERRA IVT is aggregated to have the same spatial resolution as ERA-Interim to facilitate comparisons. Both ERA-Interim and MERRA are considered "third generation" reanalysis products, which contain improvements in the representation of the global water cycle compared to previous generation products. Daily precipitation from the $1^\circ \times 1^\circ$ resolution Global Precipitation Climatology Project version 1.2 is used to quantify the impacts of ARs on global precipitation patterns. This data set is produced by optimally merging satellite retrievals and gauge analyses [Huffman *et al.*, 2001] and is regressed to the ERA-Interim resolution. The study covers the period of 1997–2014 to facilitate comparison with AR observations from satellite platforms and other studies based on similar periods.

2.2. Climate Indices

The Niño3.4 index, defined as mean SST anomalies in the equatorial central/eastern Pacific ($170\text{--}120^\circ\text{W}$, $5^\circ\text{S}\text{--}5^\circ\text{N}$), is used as an indicator of El Niño/Southern Oscillation (ENSO) conditions [Trenberth, 1997]. Monthly values of the Niño3.4 index are obtained from National Oceanic and Atmospheric Administration/Climate Prediction Center (NOAA/CPC). The phase and amplitude of the Madden-Julian Oscillation (MJO), the dominant component of tropical intraseasonal variability, are based on the commonly used Real-time Multivariate MJO (RMM) index [Wheeler and Hendon, 2004]. The RMM index defines MJO evolution as an eight-phase cycle according to the location of large-scale convective anomalies and associated changes in vertical wind shear. Daily RMM index values are obtained from the Centre for Australian Weather and Climate Research. Daily indices of the Arctic Oscillation (AO) and the Pacific/North American (PNA) teleconnection calculated by NOAA/CPC, which are based on projecting daily 1000 hPa (for AO) or 500 hPa (for PNA) geopotential height anomalies to their respective empirical orthogonal function loading patterns, are used to characterize the two prominent variability modes of the Northern Hemisphere atmosphere (<http://www.cpc.noaa.gov/products/>).

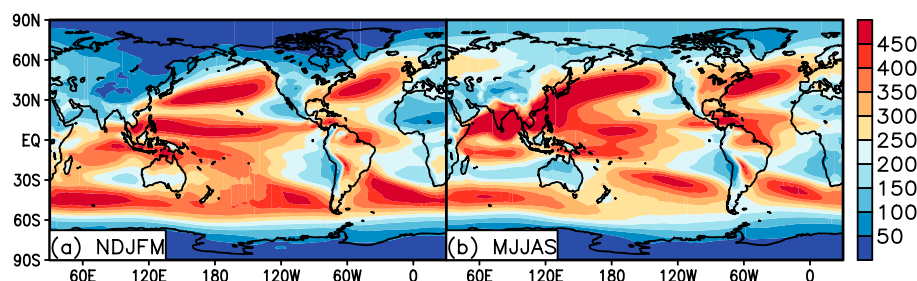


Figure 1. The 85th percentile of IVT magnitude ($\text{kg m}^{-1} \text{s}^{-1}$) at each grid cell for the period of 1997–2014. Shown are November–March (NDJFM) and May–September (MJJAS) for illustration. A total of 12 maps, for 12 overlapping 5 month seasons, is used to threshold 6-hourly IVT in the detection of ARs. Grid cells with IVT magnitude above the greater of the 85th percentile and $100 \text{ kg m}^{-1} \text{s}^{-1}$ are retained for AR detection.

For composite analysis, negative/positive phases of ENSO, AO, and PNA are defined as 0.5 standard deviation below/above zero based on their respective indices (as in *Guan et al. [2013]*). MJO composites are based on strong cases for which the magnitude of the RMM index is greater than one [*Wheeler et al., 2009*].

2.3. AR Landfall Records

Ralph et al. [2004] established the value to use satellite observation of IWV as a proxy for IVT based on the close correspondence between filamentary IWV structure and enhanced water vapor transport. They defined ARs as water vapor filaments longer than 2000 km in length, shorter than 1000 km in width, and with greater than 20 mm IWV. This definition was later used by *Neiman et al. [2008]* to create the satellite-based record of landfalling ARs onto the west coast of North America, which gives the list of dates when a 20 mm IWV “river” intersects the coastline between 32.5 and 52.5°N as observed by the Special Sensor Microwave Imager (SSM/I) and the Special Sensor Microwave Imager/Sounder (SSMIS). This record now covers the period of WY1998–2014. Using similar concept, *Lavers et al. [2011]* identified landfalling ARs associated with winter floods in Britain based on thresholding 900 hPa specific humidity with a 5 g/kg limit (which they found to be corresponding to 20 mm IWV based on linear regression). To account for reduced atmospheric water vapor content in polar areas, *Gorodetskaya et al. [2014]* identified AR landfalls associated with high snow accumulation events in East Antarctica based on saturation IWV and a formula similar to *Zhu and Newell [1998]* to extract the filamentary components. AR landfall dates reported in these three studies are used to compare with and evaluate the current AR detection.

3. AR Detection

3.1. IVT Intensity

The first step of AR detection is thresholding of IVT strength at each grid cell. The IVT threshold is a combination of a given percentile and a fixed lower limit. For each of the 12 months, the 85th percentile IVT [*Lavers et al., 2012; Nayak et al., 2014*] is calculated over all time steps during the 5 month centered on that month over the period of 1997–2014. Figure 1 shows the results for two seasons as examples. In both seasons, enhanced IVT is seen along extratropical storm tracks, with seasonal variations in strengths and locations. Enhanced equatorial IVT is reflective of the trade winds and abundance of moisture over the warm waters. In boreal summer, a band of strong IVT extends from the northern Indian Ocean into western North Pacific, which reflects the climatology of the Asian summer monsoon. IVT at high latitudes is comparatively weak where the capacity of the atmosphere to hold moisture is reduced. IVT is also weak in some continental interiors where the supply of moisture is reduced. In view of the notable seasonal and geographical variations in IVT strengths, a percentile-based threshold, conditioned on the climatology of the specific season and location, is used in our global AR detection. Similar consideration has been made in *Gorodetskaya et al. [2014]* in their design of an IWV-based AR detection scheme in Antarctica where the 20 mm IWV threshold commonly used for identification of ARs in midlatitude regions was replaced by a temperature-dependent threshold to accommodate the latitudinal gradient in moisture abundance. The 85th (or nearly identical numbers) percentile IVT has been used for AR detection focused on regions in Europe and North America

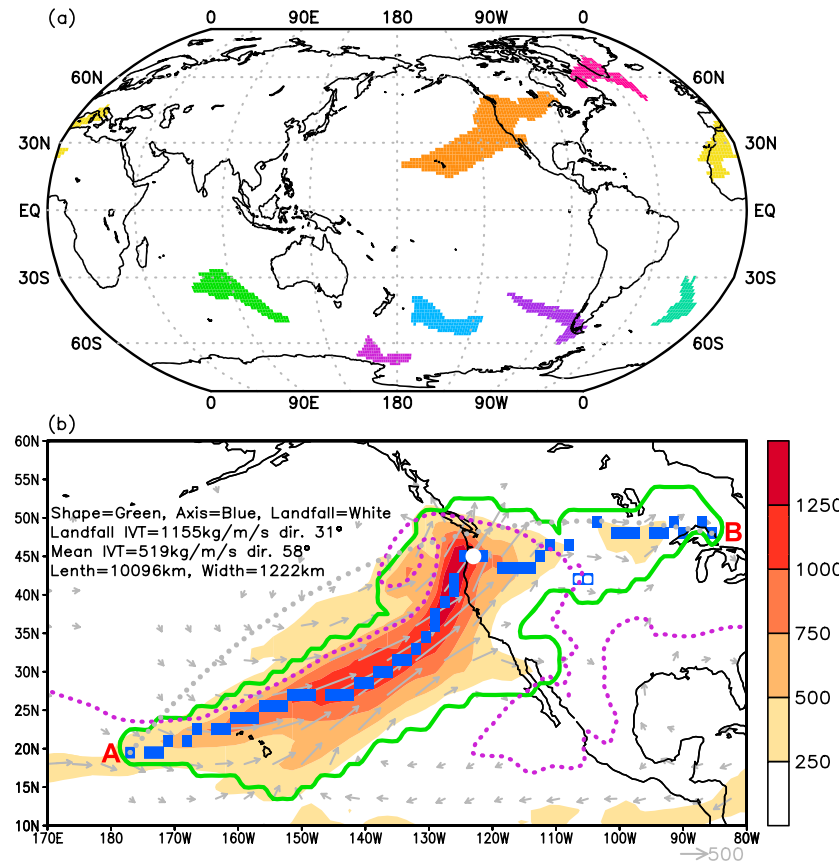


Figure 2. (a) All ARs detected at an arbitrary 6 h time step. Each color indicates a unique AR. (b) A specific AR from Figure 2a, showing the shape boundary (green), axis (blue), landfall location (white dot), and other key output of the algorithm as indicated in the upper left of the panel. Also shown are IVT ($\text{kg m}^{-1} \text{s}^{-1}$) vectors (gray arrows; not shown if the magnitude is smaller than $100 \text{ kg m}^{-1} \text{s}^{-1}$) and magnitudes (color shading), and the 20 mm contour of IWV (purple dotted) for reference. "A" and "B" mark the two grid cells with the maximum great circle (gray dotted) distance on the AR shape boundary.

with different IVT climatologies [Lavers *et al.*, 2012; Nayak *et al.*, 2014]. Sensitivity of AR detection to the IVT percentile threshold will be examined in section 3.7.

For polar areas with persistently low moisture content, IVT values corresponding to the 85th percentile are notably small and become less effective in isolating filamentary structures characteristic of ARs. For this, a fixed lower limit is used in combination with the percentile threshold, which requires IVT to be at least $100 \text{ kg m}^{-1} \text{s}^{-1}$ (corresponding to ~95th percentile in coastal Antarctica and higher percentiles farther inland). This lower limit is selected based on manual examination of its effectiveness in isolating AR-like structures in polar areas, as well as corroboration with previous results of AR detection in East Antarctica [Gorodetskaya *et al.*, 2014]. The fixed lower limit is applied to all grid cells but overwhelmed by the percentile threshold in nonpolar regions. Varying the fixed lower limit between 50 and $150 \text{ kg m}^{-1} \text{s}^{-1}$ would have no notable impact on the AR detection. A lower limit greater than $100 \text{ kg m}^{-1} \text{s}^{-1}$ would in some cases prevent landfalling ARs (such as those reported in Gorodetskaya *et al.* [2014]) from intersecting the Antarctic coast.

Application of the IVT threshold (the 85th percentile or $100 \text{ kg m}^{-1} \text{s}^{-1}$, whichever is greater) isolates contiguous regions (hereafter, objects) of enhanced IVT from the background transport, which provides the basis for subsequent considerations (Figure 2a shows the result for an arbitrary 6 h time step after all these criteria have been applied). Each object is uniquely labeled. Any object artificially cut off at the circular longitudinal boundary is properly considered and labeled as one object. Unlike in the case of IWV-based AR detection, this first step here is straightforward to implement, without the need for specific measures to prefilter the tropical moisture reservoir where IWV values are persistently high and above the IWV AR criteria [Wick *et al.*, 2013].

3.2. IVT Direction

Objects retained from the previous step are checked for the following requirements.

Coherence in IVT Direction. If more than half of the grid cells have IVT deviating more than 45° from the object's mean IVT, the object is discarded. This is aimed to filter out objects which do not exhibit a coherent IVT direction and to make a calculation of mean/characteristic IVT direction physically meaningful.

Object Mean Meridional IVT. Considering the notion that ARs transport moisture from low to high latitudes [Zhu and Newell, 1998], an object is discarded if the mean IVT does not have an appreciable poleward component ($>50 \text{ kg m}^{-1} \text{ s}^{-1}$). An object is also discarded if it straddles the equator, in which case the poleward direction is ambiguous.

Consistency Between Object Mean IVT Direction and Overall Orientation. We characterize the overall orientation of the object (i.e., the direction of the shape elongation) by the mean azimuth of the arc connecting the two boundary grid cells with the maximum great circle distance (Figure 2b, points A and B). An object is discarded if the direction of mean IVT deviates from the overall orientation by more than 45°. This is aimed to filter objects where the IVT does not transport in the direction of object elongation.

3.3. Geometry

The next step is to characterize the geometry of the objects.

Axis. The two grid cells, A and B, on the boundary of the object with the longest great circle distance are first identified (Figure 2b). Arc AB is divided into small segments, with the number of segments equal to the number of zonal or meridional (whichever is greater) grid cells between A and B. For each segment, the great circle arc perpendicular to the segment is found, and the grid cells intersected by the arc are identified. Of these grid cells, the one with maximum IVT strength is noted. The collection of the grid cells with maximum IVT, after looping through all segments, forms the AR axis (Figure 2b, blue). This method is different from the one used in Wick *et al.* [2013], which was based on the image processing technique of "skeletonization" along with other considerations. The method here is more straightforward, works with any map projection (such as the "lat-lon" projection commonly used for archiving geophysical fields on a global domain), and computationally efficient. The axis is important for calculating the AR length as well as determining landfall characteristics.

Length. The distance between the centers of each two neighboring grid cells on the AR axis is calculated, and the summation of the distances is defined to be the AR length. To prevent overestimating the AR length due to occasional noisy grid cells deviating from the overall curvature of the axis, a segment between two neighboring axis grid cells does not contribute to the calculation of AR length if they are spaced by two or more grid cells. For example, the two gaps associated with the unfilled blue boxes around 105°W, 42°N in Figure 2b are not counted in the AR length. Previous studies have used the maximum distance between any two boundary grid cells to represent the AR length, which works well for ARs with a simple elongated shape [Rutz *et al.*, 2014; Backes *et al.*, 2015]. A more sophisticated method uses the maximum combined distance between any three grid cells on the AR axis to account for some curvature of the AR [Wick *et al.*, 2013]. The method here is an attempt to better account for ARs with a highly curved or unusual shape. Based on the calculated length values, objects longer than 2000 km [Ralph *et al.*, 2004; Neiman *et al.*, 2008] are retained for subsequent consideration.

Width. The AR width is defined as the effective width of the object, calculated as the total Earth surface area of the object divided by the length. Other methods, with various degrees of complexity, have been used in previous studies to define the AR characteristic width [Wick *et al.*, 2013; Jiang *et al.*, 2014; Backes *et al.*, 2015]. In section 3.7, we discuss the sensitivity of AR detection to the geometry threshold and show that length is a more important consideration than width, consistent with the notion in Rutz *et al.* [2014] where calculation of AR width was not made. Objects with length/width ratio greater than 2 (combining the 2000 km length and 1000 km width criteria used in previous studies) are retained as the defined ARs.

3.4. Landfall

ARs determined from the previous steps are checked if they intersect the coastline, i.e., if the AR shape overlaps the land mask by at least one grid cell. We define landfalls for ARs moving from open oceans toward major landmasses. As such, islands smaller than the size of a $2.5^\circ \times 2.5^\circ$ grid cell at the equator, as well as

Table 1. The Average Number of Objects Retained After Applying Each of the AR Criteria, and the Average Number of ARs Marked as Landfalls, for Every 100 Objects in the Original Set^a

Criterion	IVT Magnitude	Coherence in IVT Direction	Object Mean Meridional IVT	Consistency Between Object Mean IVT Direction and Overall Orientation	Length and Length/Width Ratio	Length/Width Ratio
Number of objects retained or number of landfalls marked	100	98	46	42	18	4
Degree of filtering		2%	53%	10%	58%	

^aSee text for details of the applied criteria. Also indicated is the degree of filtering for each of the AR criteria, where the percentage is relative to the number of objects immediately before applying each criterion. For instance, given 100 objects identified based on the threshold for IVT magnitude, then after applying the criterion for coherence in IVT direction the number of objects is reduced to 98, thus, a filtering of 2%, and applying the criterion for object mean meridional IVT further reduces that number (98) by 53%, leaving 46 objects for subsequent criteria.

interior water bodies completely surrounded by land or nearly so are not considered. In case the AR intersects the coastline and the mean AR IVT is directed onshore, the intersecting grid cells are checked and the one with maximum onshore (i.e., directed toward an adjoining land grid cell) IVT strength is noted as the location of landfall (Figure 2b, white dot). An AR can intersect the coastline for several time steps. A time step will not be marked as landfall if the remaining length of the AR over the ocean is less than 1000 km.

3.5. AR Detection Summary

The procedure described in sections 3.1–3.4 can be summarized as three main steps: (1) extraction of the original set of “objects” based on the IVT magnitude threshold at each grid cell; (2) application of the IVT direction, length, and length/width ratio criteria to these objects, resulting in a defined set of ARs; and (3) identification of AR landfalls. Table 1 shows the average number of objects retained after applying each of the AR criteria in step 2, and the average number of ARs marked as landfall in step 3, for every 100 objects in the original set from step 1. Also shown is the degree of filtering for each of the AR criteria, where the percentage is relative to the number of objects immediately before applying each criterion. The strongest filtering (58%) is associated with the geometry criteria (mostly the length limit of 2000 km, as will be discussed in section 3.7), followed closely by the meridional IVT requirement (mean poleward component $>50 \text{ kg m}^{-1} \text{s}^{-1}$). Overall, the procedure identified 281,616 ARs in the 18 year record, with an average of 15,645 per year based on 6-hourly maps. Note that this includes the cases where a same AR system is detected multiple times at different time steps. On average 11 ARs are detected per IVT map, i.e., at any given time, for the globe. Out of these ARs, 24% are marked as landfalls, which average to two to three landfalls at any given time.

Key output from the AR detection and characterization steps is summarized with an example in Figure 2b, including the AR shape (outlined in green), axis (blue), landfall location (white dot), and length, width, mean IVT strength/direction, and IVT strength/direction at the landfall location in numbers. Landfall location and IVT strength/direction at the landfall location are set to missing for ARs that are not making landfall. In Figure 2b, it is of interest to note that the AR shape boundary based on the 85th percentile IVT (green) corresponds reasonably well with the $250 \text{ kg m}^{-1} \text{s}^{-1}$ contour (shading), which has been used as the threshold for AR detection in the western U.S. [Rutz *et al.*, 2014]. A notable difference is that the AR as detected extends farther inland in an unbroken shape than the $250 \text{ kg m}^{-1} \text{s}^{-1}$ contour of IVT. Inland penetration of ARs highlights the possibility of AR impacts in areas distant from landfall locations and the potential influence of topography on the moisture and transport [Moore *et al.*, 2012; Neiman *et al.*, 2013; Rivera *et al.*, 2014; Rutz *et al.*, 2014, 2015]. It is also noted that the detected AR is located slightly north of the 20 mm contour of IWV (purple dotted), which has been commonly used as an AR threshold in IWV-based detection. More discussion is given in section 3.6 on AR detection based on IVT versus IWV.

The capability of the algorithm in detecting ARs in east coast and tropical areas is illustrated with specific examples in Figure 3. Elongated IVT filaments reminiscent of ARs observed in extratropical/west coast areas are illustrated in these examples. However, for IWV, the elongated, filamentary structure is not as pronounced in these East Asia and eastern North America examples. For the two tropical examples, the ARs are embedded within the broad climatological band of enhanced IWV in the tropics. The potential relationship between ARs and tropical cyclones (for tropical ARs) or cyclone occlusion (for east coast ARs) is worthy of further investigation.

3.6. Evaluation

The performance of the new IVT-based AR detection algorithm is assessed by comparison to three previous studies independently conducted for three regions: western North America [Neiman *et al.*, 2008], Britain

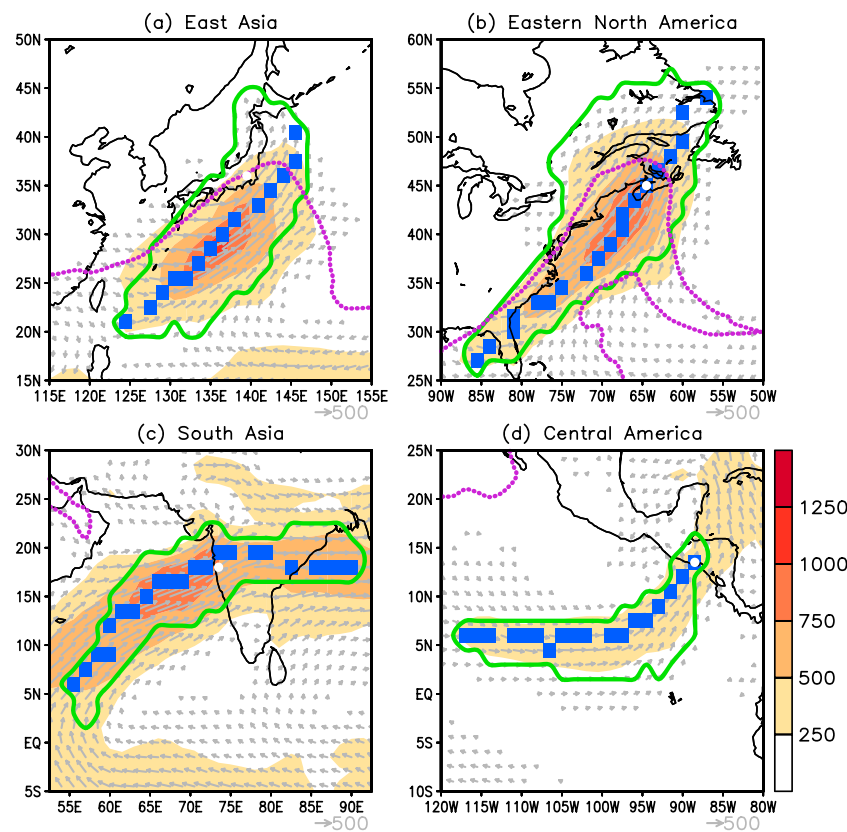


Figure 3. Examples of ARs detected in selected east coast and tropical areas. Others are as in Figure 2b.

[Lavers *et al.*, 2011], and East Antarctica [Gorodetskaya *et al.*, 2014]. Due to differences in the variables and techniques used for AR detection (Table 2), often selected to suit specific applications, the results from these studies are best viewed as complementary. AR landfall dates reported in the latter two studies are only those associated with extreme hydrological events in the respective study areas and are therefore less frequent compared to the first study. Comparison with the former two studies is only over the hydrologically important winter months. Listed in Table 2 are the variable used for AR detection, total number of landfall dates for the location and time period given, the subset of these dates that has a corresponding IVT AR landfall from the current detection within ± 1 day in the same region, and the percent agreement based on the ratio between the above two counts. The 1 day offset accommodates possible difference between the timing of IWV and IVT ARs associated with the same weather event. For example, six high snow accumulation dates studied in Gorodetskaya *et al.* [2014] occurred 1 or 2 days before an IWV AR was detected, i.e., during the IWV AR's development phase. Among these pre-IWV-AR snow events, three had an IVT AR on the same day of the snow event based on the current detection. One day timing difference was considered in Ralph *et al.* [2013] in their comparison of ARs detected based on the combination of IWV and wind information at a coastal site in California in reference to IWV ARs. Factoring in this timing difference, the percent agreement between AR landfalls detected here and in these previous studies is 94%, 89%, and 100% for western North America, Britain, and East Antarctica, respectively. Notable AR landfalls in Greenland [Neff *et al.*, 2014], Norway [Stohl *et al.*, 2008], and south-central U.S. [Moore *et al.*, 2012] are also detected, although quantitative evaluation is not conducted due to limited published record of AR landfalls in these regions. The comparison to these independent studies and techniques suggests that the current AR detection works reasonably well across regions with different climatologies.

Further comparison is made between the current IVT-based detection and the IWV-based detection in Neiman *et al.* [2008] to understand their differences in representing mean characteristics of ARs. Composite IVT and IWV are made based on cases when the two detection results agree and disagree as are corresponding composites for precipitation. As above, the comparison allows for a ± 1 day offset between

Table 2. Comparison of AR Landfall Detection Between the Current Study and Three Previous Studies Independently Conducted for Three Regions^a

Study Area	Western North America [Neiman <i>et al.</i> , 2008]	Britain [Lavers <i>et al.</i> , 2011]	East Antarctica [Gorodetskaya <i>et al.</i> , 2014]
Period	1997–2014, November–March	1997–2010, October–March	2009–2012, all months
Variable for AR detection	IWV from SSM/I and SSMIS retrievals	900 hPa specific humidity from twentieth century reanalysis project	IWV from ERA-Interim reanalysis
Intensity criterion for AR detection	20 mm	5 g/kg	IWVsat, mean + 0.2 (IWVsat, max – IWVsat, mean), where IWVsat is saturation IWV, and mean/max refers to zonal mean/maximum
Number of landfall dates	347	19 (high-impact events only)	13 (high-impact events only)
Number of landfall dates in agreement with current study	326	17	13
Percent agreement	94%	89%	100%

^aThe period listed is the overlapping period between the current study and each of the three studies. In the latter two studies, AR landfall dates are reported only for those associated with extreme hydrological events. All three studies used similar geometry criteria of approximately >2000 km long and <1000 km wide for AR detection. Number of dates in agreement with the current study is based on a ±1 day search window (see text for details). Percent agreement is based on the ratio between the number of dates in agreement and the number of landfall dates reported in the respective studies.

IWV and IVT ARs to be viewed as in agreement. The two detections agree with each other for strong ARs (Figure 4a) with strong precipitation (Figure 4d). Disagreement occurs in cases with weaker precipitation (Figures 4e and 4f), when only IWV or IVT meets the AR criteria (Figures 4b and 4c). It is noted that precipitation is stronger for cases with only IVT ARs than for cases with only IWV ARs, suggesting IVT ARs are better indicators of enhanced precipitation, consistent with the close relationship between precipitation and water vapor flux in this region [Neiman *et al.*, 2002, 2009].

The probability of AR landfall occurrence is 13% of winter days along the west coast of North America between 32.5 and 52.5°N based on IWV AR dates in Neiman *et al.* [2008] and 21% of 6-hourly winter time steps in the same region based on the current detection. The higher probability of AR landfall occurrence here is likely related to the more continuous spatiotemporal sampling of the reanalysis than for the polar orbiting satellites used for the IWV criteria, but more importantly because the definition of an AR date in Neiman *et al.* [2008] requires the AR to intersect the coastline with both the morning and the afternoon satellite observations of IWV, essentially requiring AR conditions to persist for the majority of a calendar day. With the current detection, the probability of AR landfall occurrence would be 12% of winter days in western North America (i.e., close to Neiman *et al.* [2008]) for the case when landfalls are counted only when they last for three or more consecutive 6 h time steps of a calendar day. Notably, 48 out of the 91 AR events identified in Ralph *et al.* [2013] based on hourly observations from a coastal site in California lasted no more than 12 h.

3.7. Sensitivity

Sensitivity of AR detection to the intensity and geometry thresholds and input data is assessed by examining histograms of the resulting AR IVT, lengths, and length/width ratios (Figure 5). Difference between the control and test cases is quantified by the distance between each two histograms in the N -dimensional space, where N is the number of bins. The control case (gray bars), based on IVT (from ERA-Interim) above the greater of the 85th percentile and $100 \text{ kg m}^{-1} \text{ s}^{-1}$, length >2000 km, and length/width ratio >2, provides the main results presented in this paper. Compared to the control case, increasing the IVT threshold to the 90th percentile shifts the distribution of AR IVT to the right, with increased (reduced) number of stronger (weaker) ARs (Figure 5a). Increasing the percentile threshold leads to more (fewer) ARs with smaller (larger) lengths, shifting the distribution to the left (Figure 5b). The distribution of length/width ratios is less sensitive to the IVT threshold (Figure 5c).

Relaxing the length threshold from 2000 to 1500 km leads to notable number of ARs detected in the 1500–2000 km range (Figure 5e), more ARs with smaller length/width ratios (Figure 5f), and less sensitivity in the AR IVT (Figure 5d). With the length threshold being 2000 km, AR length/width ratios are greater than 2 in nearly all cases (Figure 5f). Relaxing the length/width ratio threshold from 2 to 1 barely changes the distributions of AR IVT, length, and length/width ratio (Figures 5g–5i).

AR IVT, length, and length/width ratio are barely sensitive to the use of ERA-Interim versus MERRA as input data (Figures 5j–5l). Note that the MERRA data were regressed to the ERA-Interim spatial resolution to

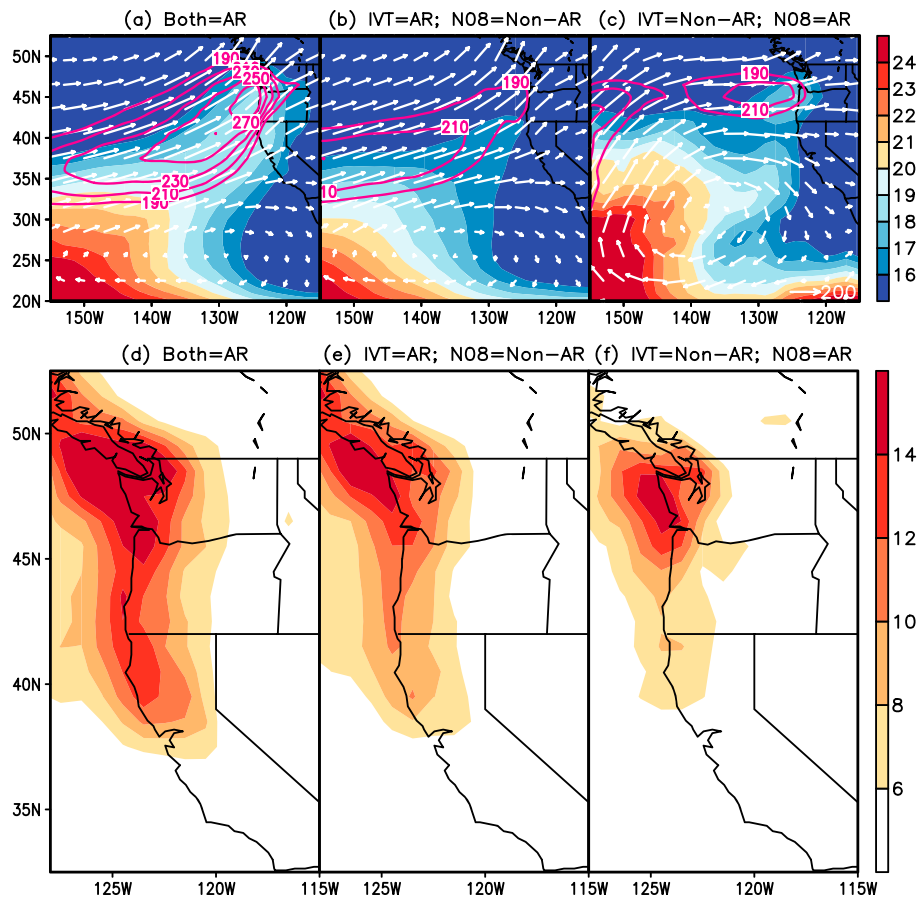


Figure 4. (a–c) Mean IVT ($\text{kg m}^{-1} \text{s}^{-1}$) vectors (white arrows) and magnitudes (magenta contours), and IWV (mm; color shading) for cases detected as landfalling ARs along the west coast of North America between 32.5 and 52.5°N during NDJFM of 1997–2014 (Figure 4a) by both the current IVT algorithm (labeled “IVT”) and the IWV-based scheme in Neiman et al. [2008] (labeled “N08”), (Figure 4b) by the IVT algorithm but not N08, and (Figure 4c) by N08 but not the IVT algorithm. (d–f) As in Figures 4a–4c but for mean precipitation (mm/d).

facilitate comparison. Out of all ARs detected with ERA-Interim, 91% have a corresponding AR in MERRA within ± 6 h that overlaps by at least 50% area. Coarsening the ERA-Interim spatial grid from $1.5^\circ \times 1.5^\circ$ to $2.5^\circ \times 2.5^\circ$ results in more less elongated ARs, shifting the distribution of length/width ratios to the left (Figure 5l). Coarser spatial grids tend to smooth out the IVT field and may therefore damp the narrowness of ARs. Coarsening the spatial grid has a weaker effect on the AR length (Figure 5k) and further weaker effect on AR IVT (Figure 5j). Temporally averaging the 6-hourly ERA-Interim IVT to 12-hourly reduces the number of maps available for AR detection by 50%. For this test case, the histograms are scaled by 2 to facilitate comparison with other cases. The temporal averaging only slightly shifts the distributions of AR IVT, length, and length/width ratio to the left (Figures 5j–5l). The analysis in Figure 5 suggests that among the intensity and geometry thresholds considered, the length threshold leads to the most sensitivity in AR detection. Regarding input data, the spatial resolution, compared to the temporal resolution and the selection of a specific reanalysis data set, leads to the largest sensitivity in AR detection.

4. Global Climatology

4.1. Basic Characteristics

Basic geometry, location, and IVT characteristics of the detected ARs are shown by the histograms in Figure 6. AR length has a monotonically decreasing probability distribution, with a median of ~ 3665 km (Figure 6a). ARs longer than 5000 km are not uncommon. In some cases, ARs can be longer than 10,000 km. AR width has a positively skewed distribution, with a median of ~ 564 km (Figure 6b).

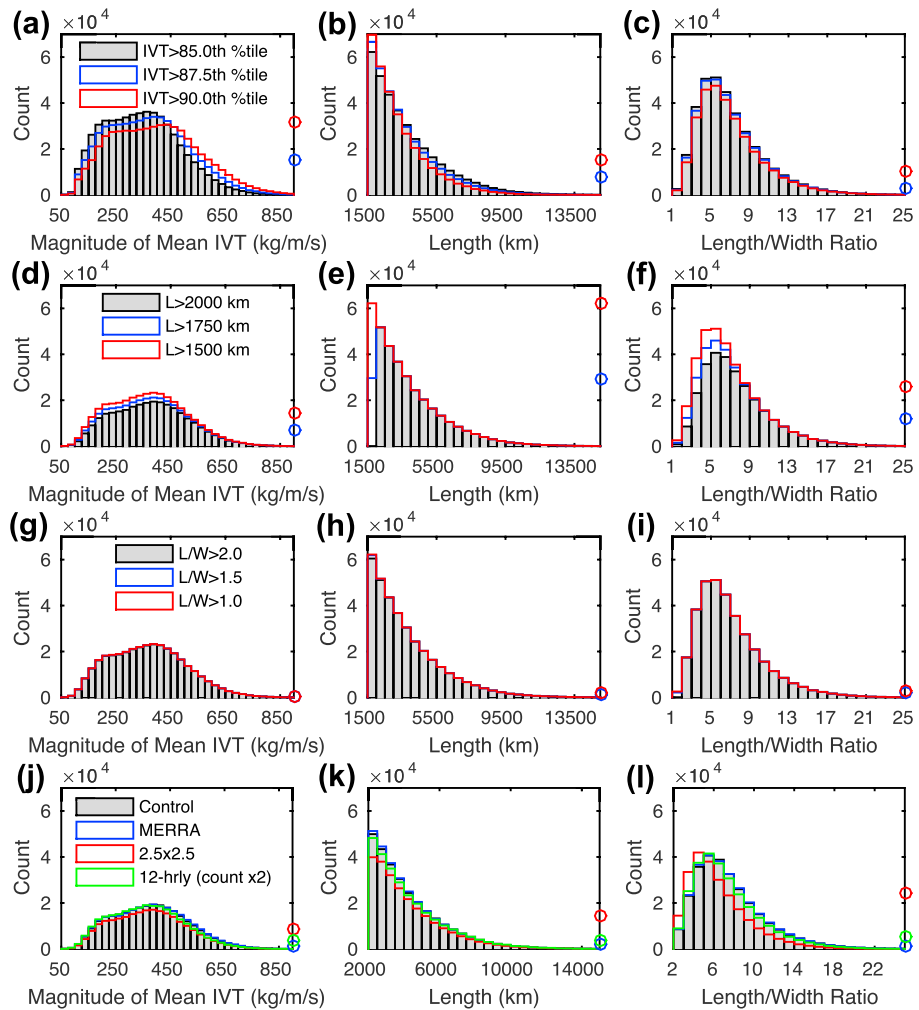


Figure 5. Sensitivity of AR detection to the thresholds of (a–c) IVT percentile, (d–f) length, (g–i) length/width ratio, and (j–l) the input data. In each row, sensitivity is examined for histograms of AR IVT, length, and length/width ratio. In Figures 5j–5l, the legend indicates the only aspect of each test case different from the control; the latter is based on 6-hourly, $1.5^\circ \times 1.5^\circ$ ERA-Interim IVT. In each panel, color circles on the right ordinate indicate the distance between the control and test case histograms in the N -dimensional space, where N is the number of bins. Calculations are based on all months of 1997–2014.

The characteristic AR length and width, represented by the median numbers, are in broad consistency with previous characterization of the AR geometry [Ralph and Dettinger, 2011]. AR length/width ratio also has a positively skewed distribution, with a median of ~ 7 (Figure 6c). The relative narrowness of ARs, compared to the length, is notable.

Geographically, ARs are the most probable to occur in the midlatitudes (Figures 6d–6f), with a roughly symmetric distribution in each hemisphere, and a median latitude of the AR centroid, equatorward end, and poleward end being $\sim 40^\circ$, $\sim 30^\circ$, and $\sim 50^\circ$, respectively. This is consistent with the common notion that ARs are primarily an extratropical phenomenon. The latitudinal distribution of AR locations, meanwhile, does highlight the global footprints of ARs.

AR median IVT is $\sim 374 \text{ kg m}^{-1} \text{s}^{-1}$, with a modest fraction (20%) of ARs having mean IVT weaker than $250 \text{ kg m}^{-1} \text{s}^{-1}$ (Figure 6g). AR IVT is predominantly directed northeastward in the Northern Hemisphere with a median azimuth of $\sim 56^\circ$ (azimuth is 0° if IVT is directed due north), and southeastward in the Southern Hemisphere with a median azimuth of $\sim 121^\circ$ (Figure 6h). The two angles are approximately symmetric about the equator and indicate that AR IVT typically has a stronger eastward component than poleward component. ARs with westward directed IVT (azimuth $> 180^\circ$) are uncommon.

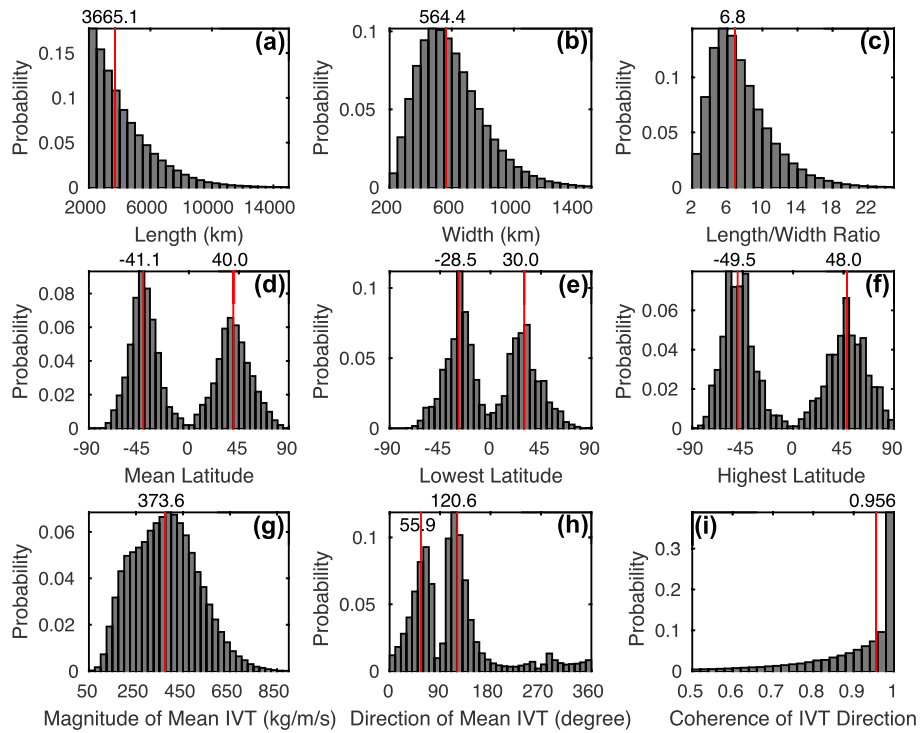


Figure 6. Histograms of basic characteristics of ARs detected over all months of 1997–2014. The red lines in each panel indicate the median (in case of one line) or the median in each hemisphere (in case of two lines).

Coherence of IVT directions within an AR is calculated as the fraction of AR grid cells with IVT directed within 45° of the mean AR IVT (Figure 6). The median fraction of 0.96 indicates that the ARs detected have highly coherent IVT direction. The fraction is rarely less than 0.8. For 95% of the ARs detected, 75% of the total IVT is contained in the layer below ~ 600 hPa (not shown; although see Figure 8c), consistent with previous finding based on landfalling ARs over the northeastern Pacific that AR IVT is largely concentrated in the lowest few kilometers above surface [Ralph et al., 2005; Neiman et al., 2009].

4.2. Global Distribution

Shown in Figure 7a is the global distribution of AR frequency and mean AR IVT, calculated independently for each grid cell based on the detected AR shapes. For any given time step, only those grid cells within the AR shape boundaries are included for calculation. ARs occur more frequently in midlatitude ocean basins than over land and other latitudes, with centers of maximum frequency located in extratropical North Pacific/Atlantic, southeastern Pacific, and South Atlantic. AR frequency is the lowest in the polar areas. In interior Antarctica, no ARs are detected over the 18 year period (white shading in Figure 7a). Along the west coast of North America, the north-south gradient in AR frequency and the reduction of AR frequency toward the continental interiors are in broad consistency with Rutz et al. [2014]. Compared to their study, AR frequency here is considerably higher in the interior western U.S., because the AR shape determined by the 85th percentile IVT extends farther inland than the contour of $250 \text{ kg m}^{-1} \text{ s}^{-1}$ (Figure 2b). AR IVT is strongest over the extratropical ocean basins and directed eastward and poleward, consistent with the finding in Zhu and Newell [1998] based on 3 years of data and a formulation to extract AR IVT without explicit consideration of AR geometry.

ARs account for 84% (88%) of the total meridional IVT and 8% (11%) of the zonal circumference between 30° and 50° in the Northern (Southern) Hemisphere (Figures 7b and 7c). The AR fractional IVT is slightly lower than shown in Zhu and Newell [1998; see their Figure 6], which could be related to differences in the data sources and analysis periods. The AR fractional zonal-scale matches Zhu and Newell [1998] very well.

Coherence of IVT directions between ARs occurring at different times in the same grid cell is calculated as the fraction of times with AR IVT directed within 45° of the time mean AR IVT. The direction of AR IVT is highly

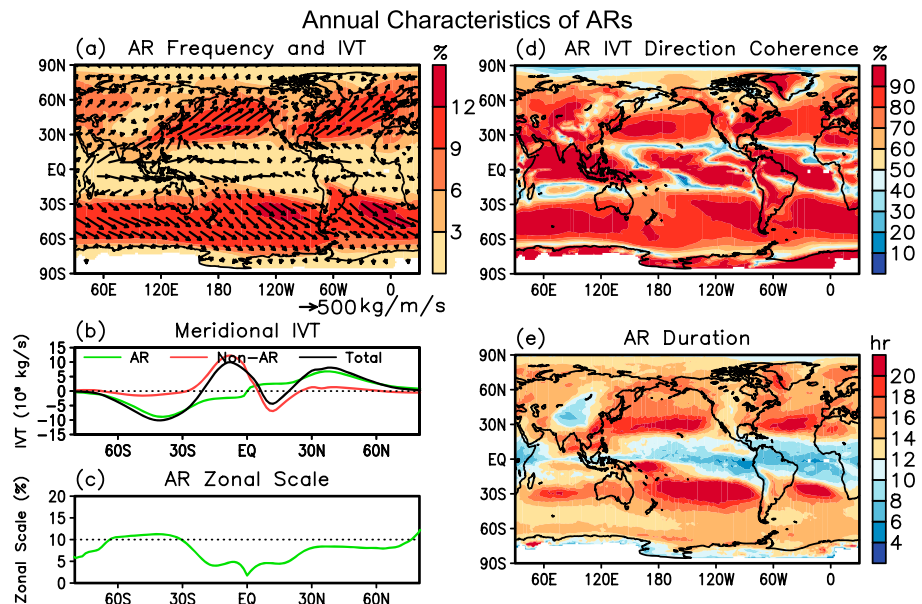


Figure 7. (a) AR frequency (percent of time steps; shading) and mean AR IVT ($\text{kg m}^{-1} \text{s}^{-1}$; arrows) at each grid cell. White shading in limited areas indicates no AR detected over the analysis period. (b) Zonally integrated meridional IVT (kg s^{-1}) associated with AR transport (green), non-AR transport (red), and their combination (black). (c) Integrated AR zonal scale expressed as the fraction of the total zonal circumference at given latitudes. (d) Coherence in the direction of AR IVT at each grid cell, calculated as the percent of AR time steps when the direction of IVT fall within 45° of the time mean AR IVT as shown in Figure 7a. (e) Mean duration (hour) of ARs at each grid cell. Calculations are based on all months of 1997–2014.

coherent over the majority of the globe, with exceptions in limited areas in the tropical and polar regions and a few continental interiors in the extratropics (Figure 7d).

Mean duration of ARs is calculated at each grid cell as the average number of hours (based on 6-hourly time steps) a grid cell stays continually within an AR, i.e., from a Eulerian perspective. This way of calculating the AR duration is most relevant to understanding the potential impact of ARs in a given location [Ralph *et al.*, 2013; Rutz *et al.*, 2014]. Tracking an AR over its life cycle is not conducted in this study. AR duration is longest in most extratropical ocean basins (Figure 7e). In this regard, regions with more AR occurrences tend to have more persistent ARs as well (comparing Figures 7a and 7e). Based on hourly observations from an AR observatory at Bodega Bay, California, for a total of 91 AR events, Ralph *et al.* [2013] calculated the mean AR duration to be 16 h, which matches exactly with the current calculation at the grid cell containing the observation site. Considering the mean AR duration for a given location is determined by the typical propagation speed of the passing AR system and AR width, the above agreement suggests that the mean AR width is reasonably characterized by the detection algorithm in this region.

4.3. Landfalls

AR landfalls are most frequent along the west coasts of North America, southern South America, and Europe (Figure 8a). AR landfalls and their association with extreme precipitation/floods in western North America and Europe have been extensively studied. Recent studies have documented AR landfalls in the central Andes in South America [Viale and Nuñez, 2011; Viale *et al.*, 2013]. A notable number of AR landfalls occur in Greenland and Antarctica, where the impacts of ARs on snow and ice sheets are recently becoming recognized [Gorodetskaya *et al.*, 2014; Neff *et al.*, 2014]. AR landfalls along the Gulf of Mexico have been linked to floods in the central U.S. [Moore *et al.*, 2012; Lavers and Villarini, 2013a]. Considerable AR landfalls also occur in regions where ARs have received less scientific attention, including South/East Asia, Australia and New Zealand, northeastern North America, central America/Caribbean, and northwestern/southwestern Africa.

Mean vertical distribution of horizontal water vapor fluxes at AR landfalls is examined for six representative locations with enhanced landfall frequencies, namely, California, British Columbia, Britain, Chile, Greenland, and the Antarctic Peninsula (Figure 8a, plus signs). Water vapor fluxes have a sharp peak around 900 hPa

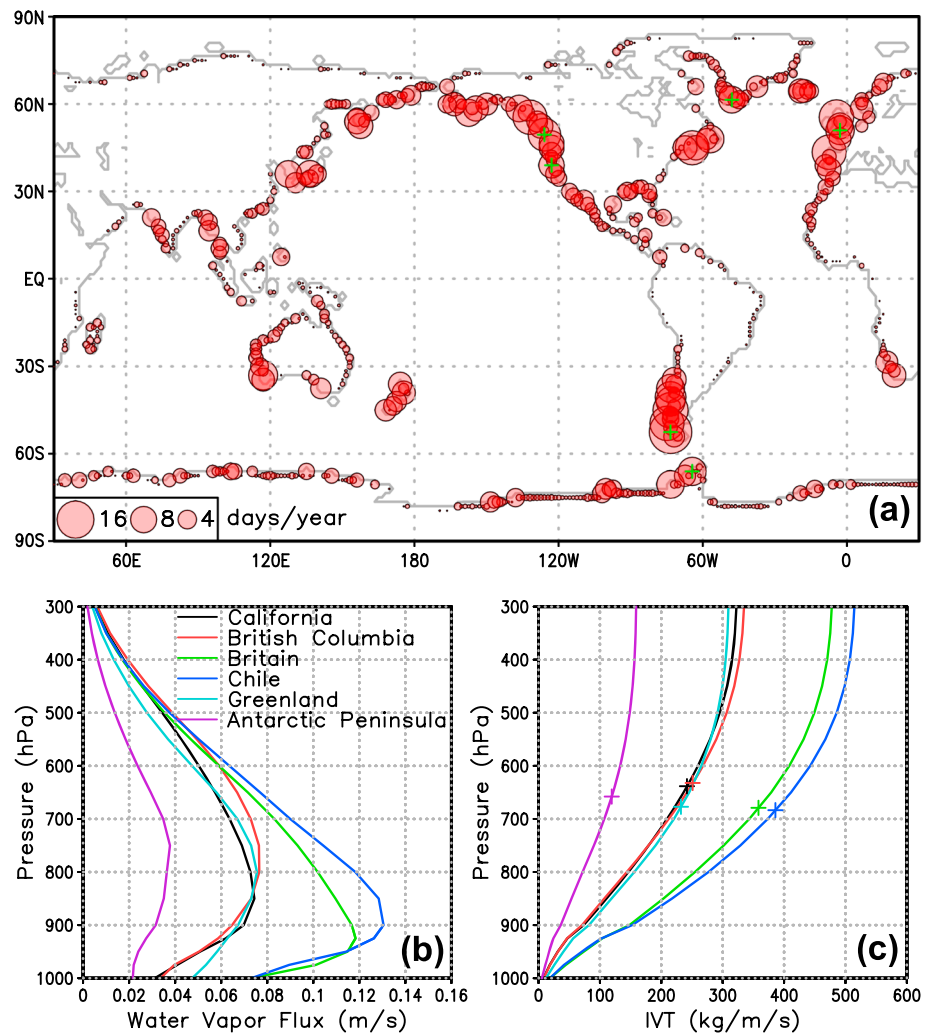


Figure 8. (a) Frequency (days per year) of AR landfalls based on all months of 1997–2014. The frequency values in days per year were obtained by multiplying the fraction of 6-hourly time steps with AR landfalls (i.e., probability of landfall occurrence) by 365.2425. Green plus signs indicate locations with notable AR landfall frequencies selected for the analysis in Figures 8b and 8c. (b) Mean vertical profile of horizontal water vapor fluxes (m s^{-1}) at six locations as marked in Figure 8a. (c) Mean cumulative horizontal water vapor fluxes ($\text{kg m}^{-1} \text{s}^{-1}$) between 1000 hPa and each pressure level for the six locations. The plus signs indicate the level below which 75% of the column total IVT is contained.

for the cases of Britain and Chile, less sharp peaks near 850 hPa for California, near 800 hPa for British Columbia and Greenland, and a smoother peak around 750 hPa for the Antarctic Peninsula (Figure 8b). The magnitude of AR water vapor fluxes also varies with locations, with mean IVT ranges between about 150 and 500 $\text{kg m}^{-1} \text{s}^{-1}$ among the six locations (Figure 8c). For these locations, the majority (i.e., >75%) of the IVT is contained below ~650 hPa (Figure 8c, plus signs), highlighting the low-level nature of ARs across different regions.

4.4. Seasonality

Seasonal climatologies of AR frequency and precipitation in November–March versus May–September are shown in Figure 9. The two extended seasons are hydrologically important to a number of west coast areas of the midlatitude continents where the two seasons exhibit contrasting dry/wet conditions characteristic of the Mediterranean climate. As earlier, calculations are independently conducted for each grid cell based on the detected AR shapes. In that regard, AR precipitation here specifically refers to precipitation that falls within the AR shape boundaries. The largest seasonal variations in AR frequency occur in the northeastern Pacific extending toward western U.S. and in southeastern Pacific extending to central Chile (Figures 9a and 9b), with the amplitude of seasonal variations above one third of the annual mean (Figure 9c). In both regions, AR frequencies

Seasonality of AR Frequency and Precipitation

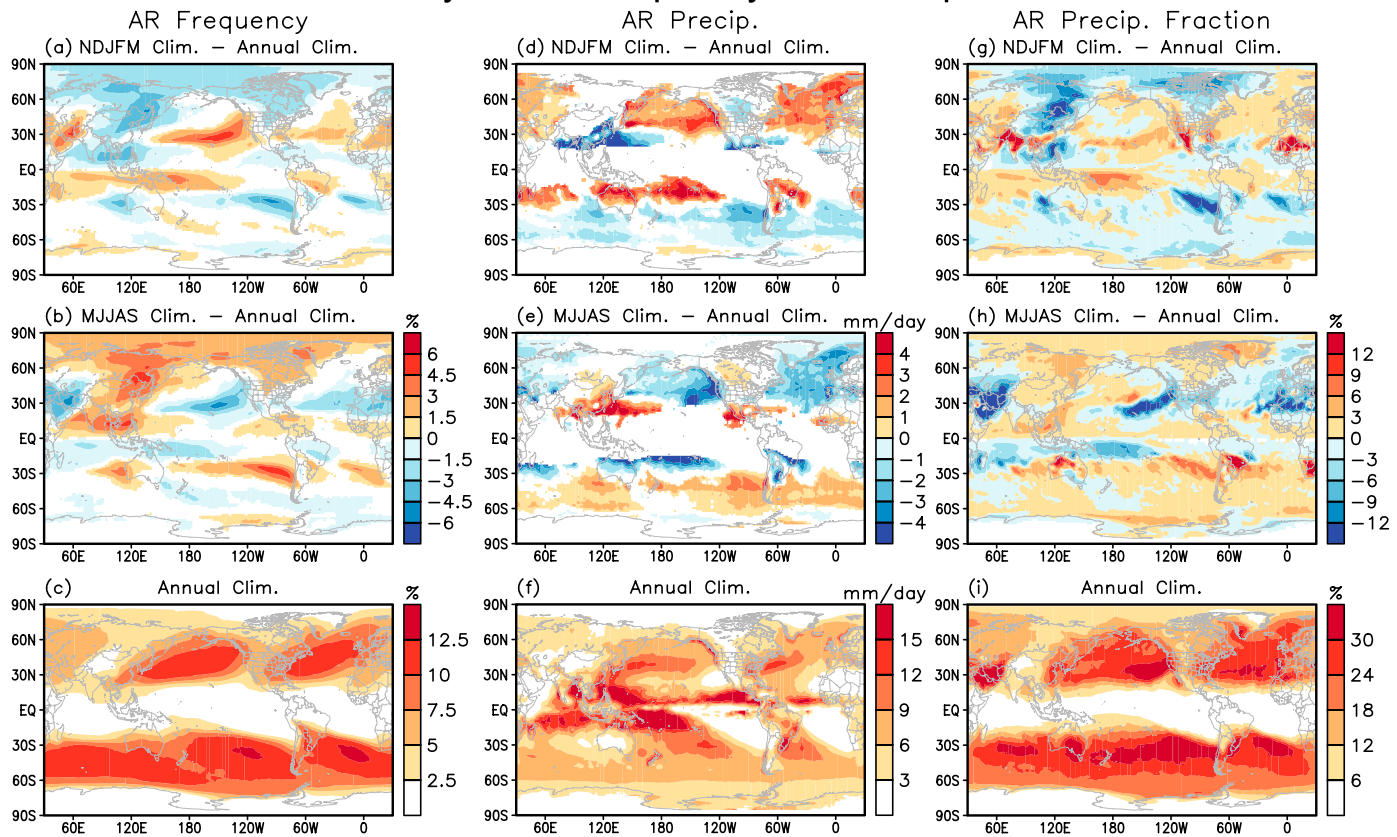


Figure 9. (a–c) AR frequency (percent of time steps) in (Figure 9a) NDJFM and (Figure 9b) MJJAS with (Figure 9c) the annual AR frequency subtracted. (d–f) As in Figures 9a–9c but for AR precipitation (mm/d). (g–i) As in Figures 9a–9c but for AR precipitation fraction (percent of total precipitation). In Figures 9a, 9b, 9d, and 9e, values are shown only if they are statistically significant at the 95% level based on two-tailed z test, and the number of samples contributing to the calculation is greater than 200. Note that Figure 9c is the same as the color shading in Figure 7a but with a slightly different color bar—the former mapping white to regions of very low AR frequency.

are increased in their respective winter seasons. Considering the areas where ARs frequently make landfalls (see Figure 8a), the largest seasonal variations in AR precipitation occur along the west coast of North America (Figures 9d and 9e), where AR precipitation is enhanced in winter by over one third of the annual mean (Figure 9f). The seasonal contrast in AR precipitation patterns is in broad consistency with Neiman *et al.* [2008] that focused on landfalling ARs along the west coast of North America. AR precipitation exceeds 30% of the total precipitation in a number of extratropical areas (Figure 9i). The results are largely consistent with previous studies that examined AR precipitation fractions in various areas of western/central/eastern North America and West Europe [Guan *et al.*, 2010; Dettinger *et al.*, 2011; Rutz and Steenburgh, 2012; Rutz *et al.*, 2014; Lavers and Villarini, 2015]. AR precipitation fractions exhibit strong seasonal variations along the west coasts of North and South Americas (Figures 9g and 9h), where increased AR precipitation fractions in their respective winter seasons are consistent with higher AR frequency and stronger AR precipitation there in winter. Interesting seasonal contrasts in AR frequency and precipitation are also seen in some east coast areas, in particular East Asia, where the anomalies exhibit opposite signs compared to the other side of the Pacific and may have different implications to seasonal precipitation under the monsoonal climatology.

4.5. Climate Modulation

A previous study found a close relationship between the frequency of landfalling ARs in California and two prominent modes of climate variability in the Northern Hemisphere atmosphere, namely, the AO and the PNA [Guan *et al.*, 2013]. In that regard, the unusually high snow accumulation in California's Sierra Nevada during the 2010/2011 winter was primarily attributed to enhanced AR frequency favored by circulation anomalies associated with the joint phasing of negative AO and negative PNA in an extended period of that

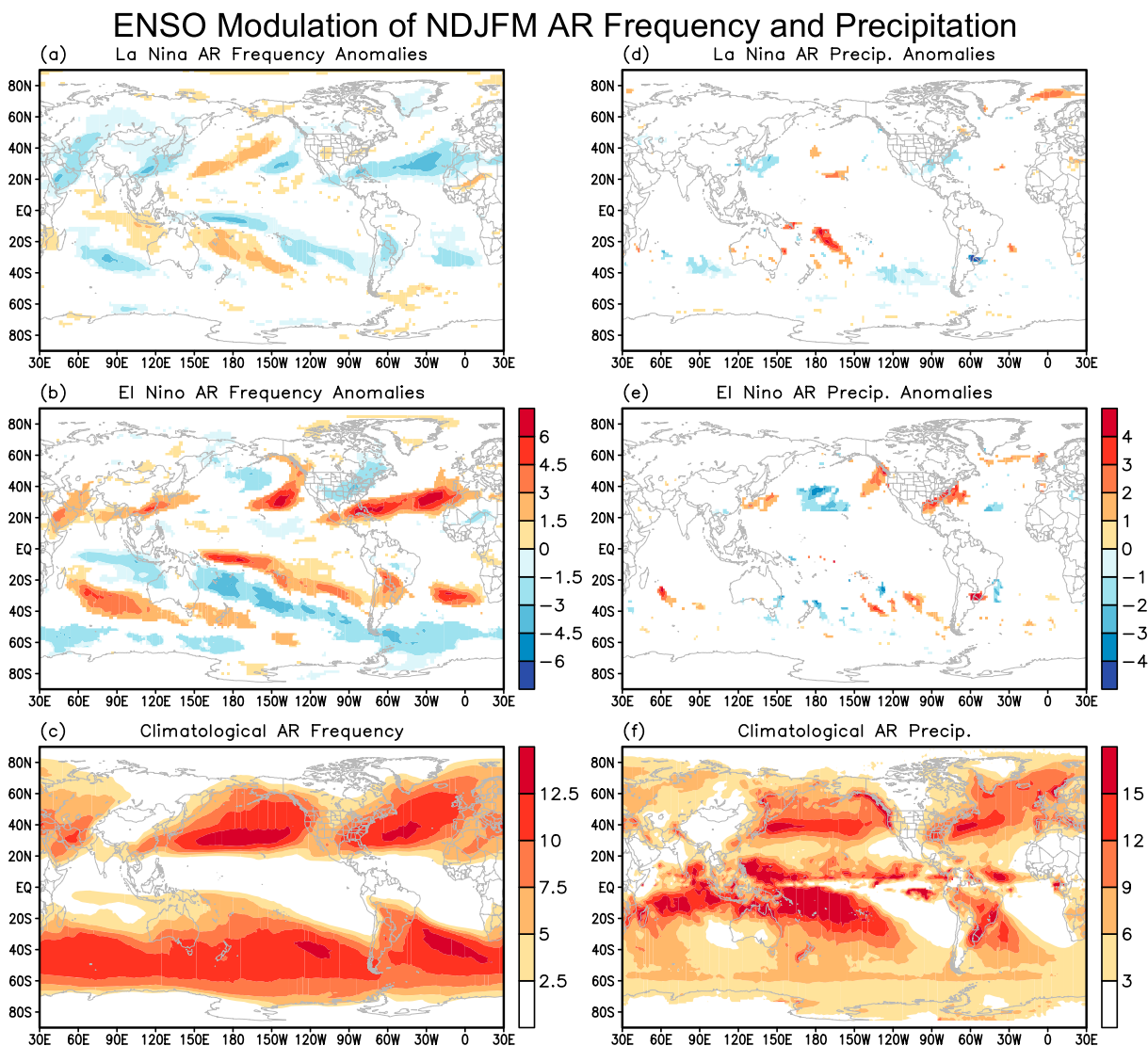


Figure 10. (a and b) Composite NDJFM AR frequency anomalies (percent of time steps) during (Figure 10a) La Niña and (Figure 10b) El Niño conditions. (c) NDJFM climatology of AR frequency, based on which the composite anomalies in Figures 10a and 10b are calculated. (d–f) As in Figures 10a–10c but for AR precipitation (mm/d). In Figures 10a, 10b, 10d, and 10e, values are shown only if they are statistically significant at the 95% level based on two-tailed z test, and the number of samples contributing to the calculation is greater than 200.

winter. In that analysis, ENSO was not found to strongly modulate AR frequency in California. Another study found that the occurrence of high-impact AR landfalls in California's Sierra Nevada is most favored by MJO phase 6 compared to other phases, when the MJO convective anomalies are located in the far western Pacific [Guan et al., 2012].

Making use of the global AR detection here, the analyses in the above two California-focused studies are extended to the Northern Hemisphere for AO and PNA and both hemispheres for ENSO and MJO. The impacts of these modes on AR frequency and precipitation intensity are examined with composite anomalies during different phases of these modes relative to the AR climatology. Only the winter months (November–March) are considered, during which the four modes are the most active and potentially more influential to AR activities.

El Niño conditions increase AR frequency in a number of subtropical/extratropical regions, with the strongest anomalies located in the northeastern Pacific, North Atlantic, and the Gulf of Mexico/Caribbean, and slightly weaker but coherent anomalies in the southern Indian Ocean, the South Pacific convergence zone extending into South America, and South Atlantic (Figure 10b). The anomaly patterns are largely reversed during La Niña (Figure 10a). The magnitudes of the anomalies are coherent and notable in many regions

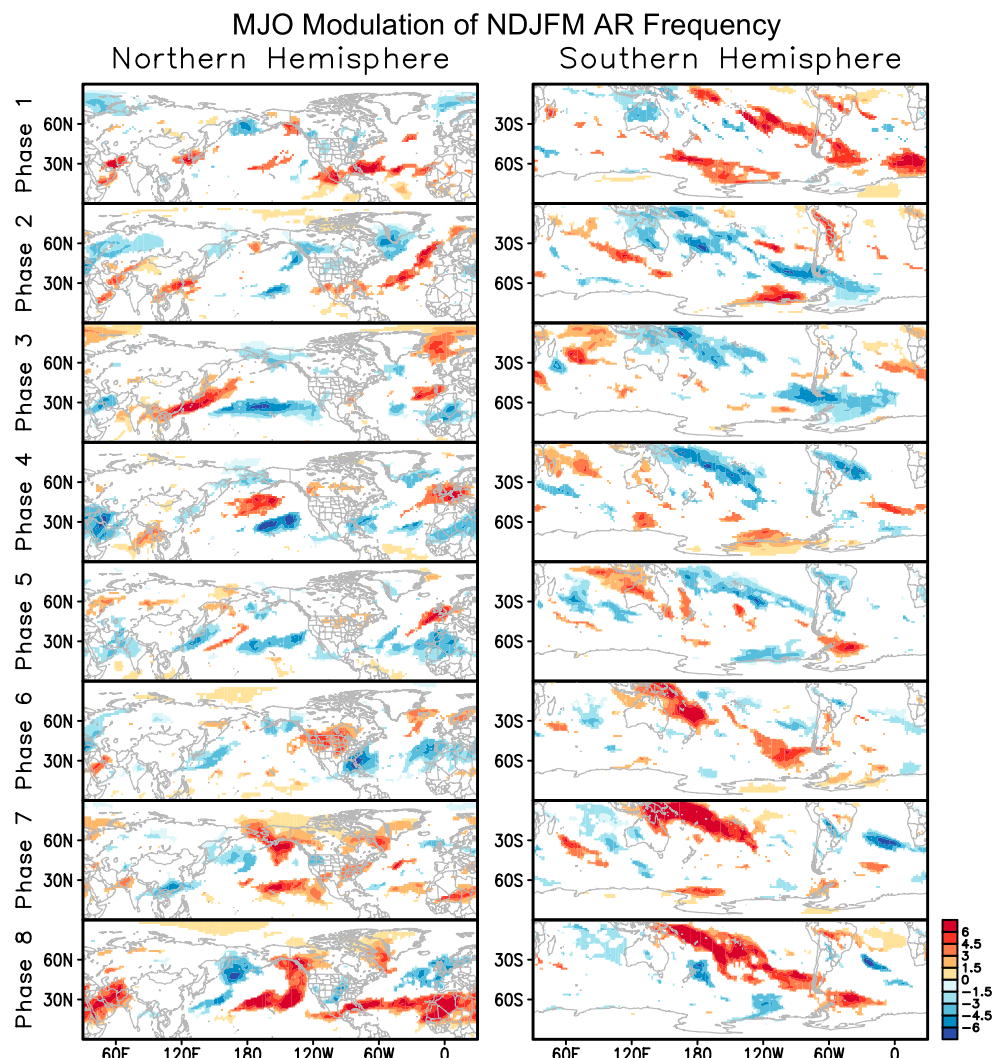


Figure 11. Composite NDJFM AR frequency anomalies (percent of time steps) relative to the NDJFM climatology during each phase of the MJO. The two hemispheres are shown separately in two columns to improve the visualization. Values are shown only if they are statistically significant at the 95% level based on two-tailed z test, and the number of samples contributing to the calculation is greater than 50.

compared to the climatology (Figure 10c; see also Figure 15a). Consistent with the landfall-focused analysis in Guan *et al.* [2013], the influence of ENSO on AR frequency is weak in/near California. Focusing on the areas where ARs frequently make landfalls (see Figure 8a), the most notable impact of ENSO on AR precipitation is seen in/offshore the U.S. Pacific Northwest and western Canada, where AR precipitation is increased during El Niño (Figure 10e).

The MJO is the dominant component of tropical intraseasonal variability [Madden and Julian, 1971, 1972] characterized by large-scale, eastward propagating convective anomalies along the equatorial band with typical periods of 40–50 days [e.g., Matthews, 2000]. The MJO interacts with phenomena on multiple time-scales with far-reaching impacts, including those on ARs (e.g., the case study in Ralph *et al.* [2011]). In the North Pacific, MJO-related AR frequency anomalies are marked by propagation of positive anomalies from East Asia to south of the Aleutian Islands during phases 1–4, followed by propagation of negative anomalies during phases 5–8 in this region (Figure 11, left). Positive anomalies offshore the Pacific Northwest of U.S./Canada during phase 6 (consistent with Guan *et al.* [2012] that focused on California), and more pronounced ones south of Alaska/western Canada during phases 7–8 are notable. Positive anomalies are also seen propagating from tropical North America to North Europe during phases 1–4, followed by propagation of somewhat less coherent

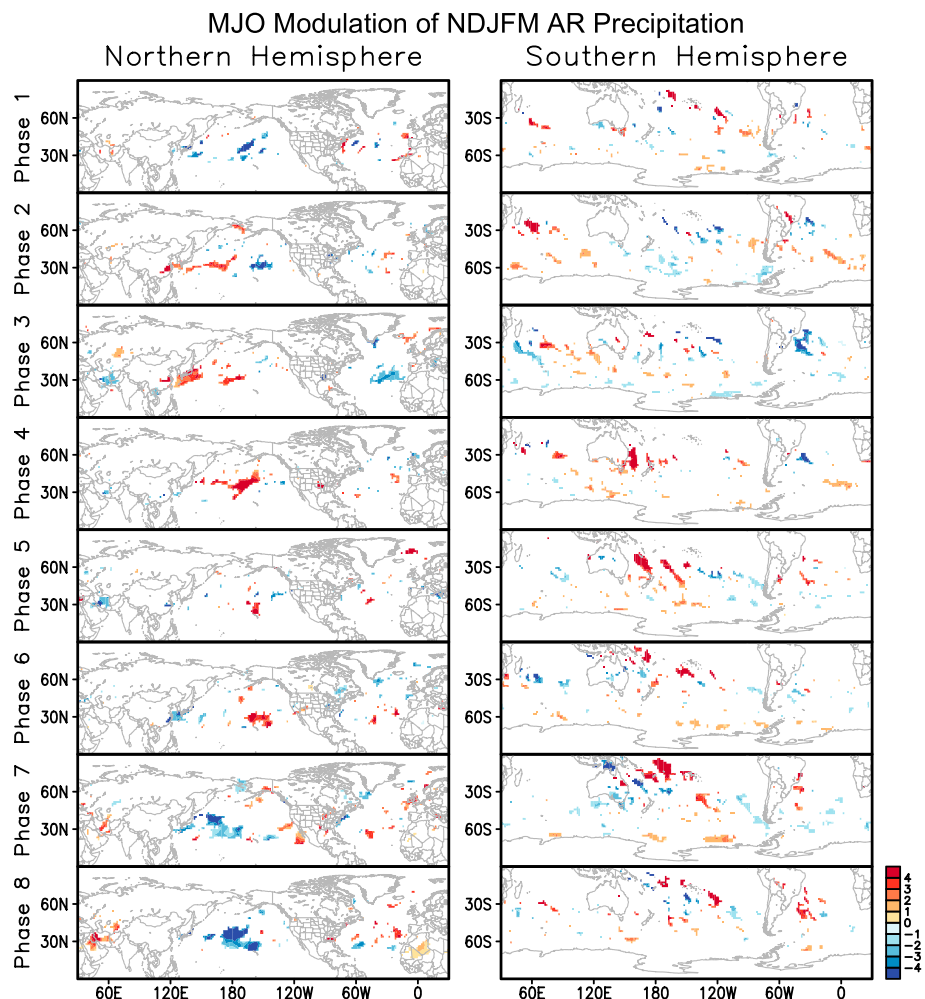


Figure 12. As in Figure 11 but for AR precipitation anomalies (mm/d).

negative anomalies in this region during phases 5–8. In the Southern Hemisphere, AR frequency anomalies are characterized by eastward propagation of an anomaly band that at the peak stage extends from the Maritime Continent all the way to east of the Antarctica Peninsula (Figure 11, right). Positive AR precipitation anomalies are seen propagating from East Asia to offshore California during phases 2–7, accompanied by propagation of negative anomalies in this region during phases 6–3 (Figure 12, left; note that MJO phase 8 is followed by phase 1, by definition). Eastward propagation of AR precipitation anomalies is also seen in the Southern Hemisphere, which is most notable between Australia and French Polynesia during phases 4–7 (Figure 12, right). It is noted that the influence of the MJO on AR frequency and precipitation is often located away (downstream) from the longitudinal location of the MJO convective anomalies, a connection also found in previous studies of MJO influence on ARs [Ralph *et al.*, 2011; Guan *et al.*, 2012].

The AO is characterized by sea level pressure anomalies of one sign in the Arctic area and anomalies of opposite sign in the surrounding extratropical areas [Thompson and Wallace, 1998]. During the negative phase of AO, AR frequency is enhanced in the subtropical Pacific offshore western U.S., subtropical North Atlantic extending to South Europe, and in Labrador Sea/western Greenland, and meanwhile, AR frequency is reduced in North Europe (Figure 13a). The strong and coherent anomalies in the subtropical North Atlantic are remarkable, where the magnitude of the anomalies is several times the amplitude of the seasonal cycle (comparing Figures 13a and 9a). The negative phase of AO is associated with weakened midlatitude westerly winds, which favors southward excursion of cold Arctic air and associated storminess [Jeong and Ho, 2005] that may potentially contribute to AR activities. AR frequency anomalies are largely reversed during the positive phase of AO (Figure 13b). Increased AR frequency offshore California during negative AO is in agreement

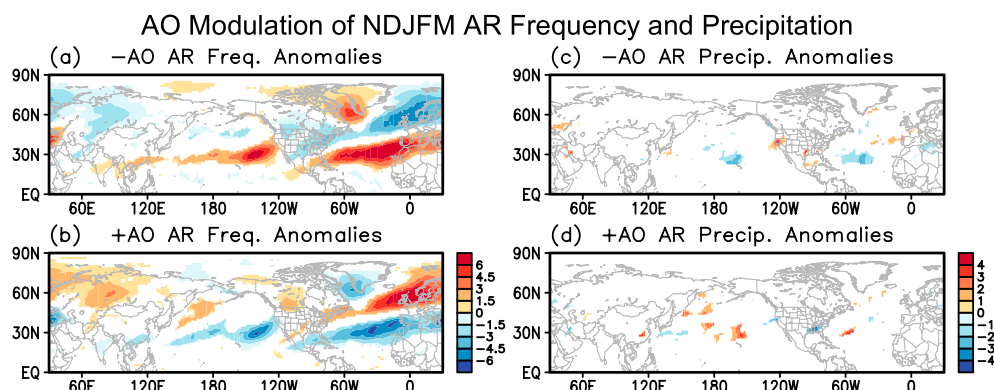


Figure 13. As in Figures 10a, 10b, 10d, and 10e but for the AO.

with *Guan et al.* [2013] based on an independent data set of landfalling ARs. The north-south seesaw pattern of AR frequency in Europe between the two phases of AO is consistent with the finding in *Lavers and Villarini* [2013b] for the North Atlantic Oscillation, a close relative of the AO with similar regional circulation patterns. Localized anomaly in AR precipitation is seen in/offshore northern California, where it is increased (decreased) during negative (positive) AO (Figures 13c and 13d).

The PNA is characterized by a wave train pattern with two positive and two negative anomaly centers linking the Pacific Ocean and the North American continent [Wallace and Gutzler, 1981]. The impact of PNA on AR frequency is such that AR frequency is increased to the southeast (northwest) of the low- (high-) pressure centers, consistent with the direction of wind anomaly implicated by the pressure systems (Figures 14a and 14b). Increased AR frequency in California during negative PNA is consistent with *Guan et al.* [2013] based on an independent data set of landfalling ARs. AR precipitation is decreased (increased) offshore northern California during negative (positive) PNA (Figures 14c and 14d).

In/offshore California, the sign of AR precipitation anomalies associated with each phase of AO and PNA (Figures 13c, 13d, 14c, and 14d) is consistent with the modulation of AR IVT strengths by the two modes shown in *Guan et al.* [2013; their Figure 9]. That study also showed that landfalling ARs in California have much stronger IVT during El Niño than La Niña. Here it is shown that with respect to the resulting AR precipitation, ENSO has a larger and more significant impact in the U.S. Pacific Northwest and western Canada than in California.

Compared to the impact on AR frequency, the impact of the four large-scale climate modes on AR precipitation is highly localized (Figures 10–14) and the strength relative to the climatology is often less pronounced (Figure 15), suggesting that regional- and local-scale variability may play important roles in modulating AR precipitation in addition to the large-scale conditions. The impacts of regional/local circulation patterns on winter AR frequencies in Europe have been examined in two studies [*Lavers et al.*, 2012; *Ramos et al.*, 2015], which have implication on the impacts on AR precipitation. Further investigations are needed to better understand the range of processes that determine AR precipitation in different regions and seasons.

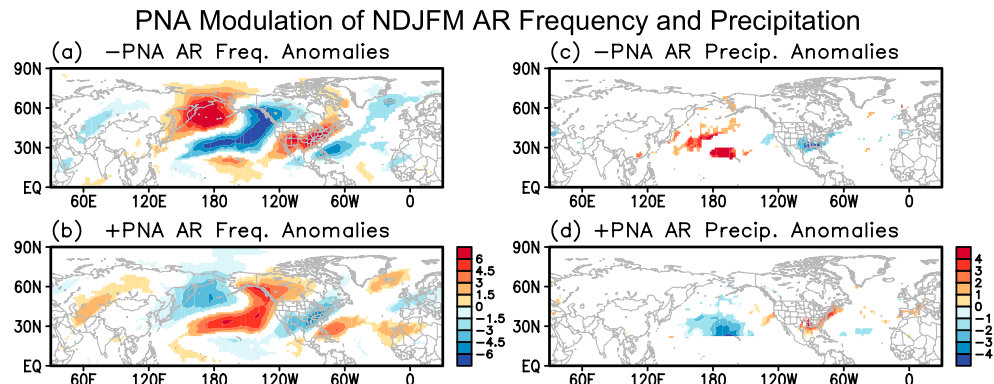


Figure 14. As in Figures 10a, 10b, 10d, and 10e but for the PNA.

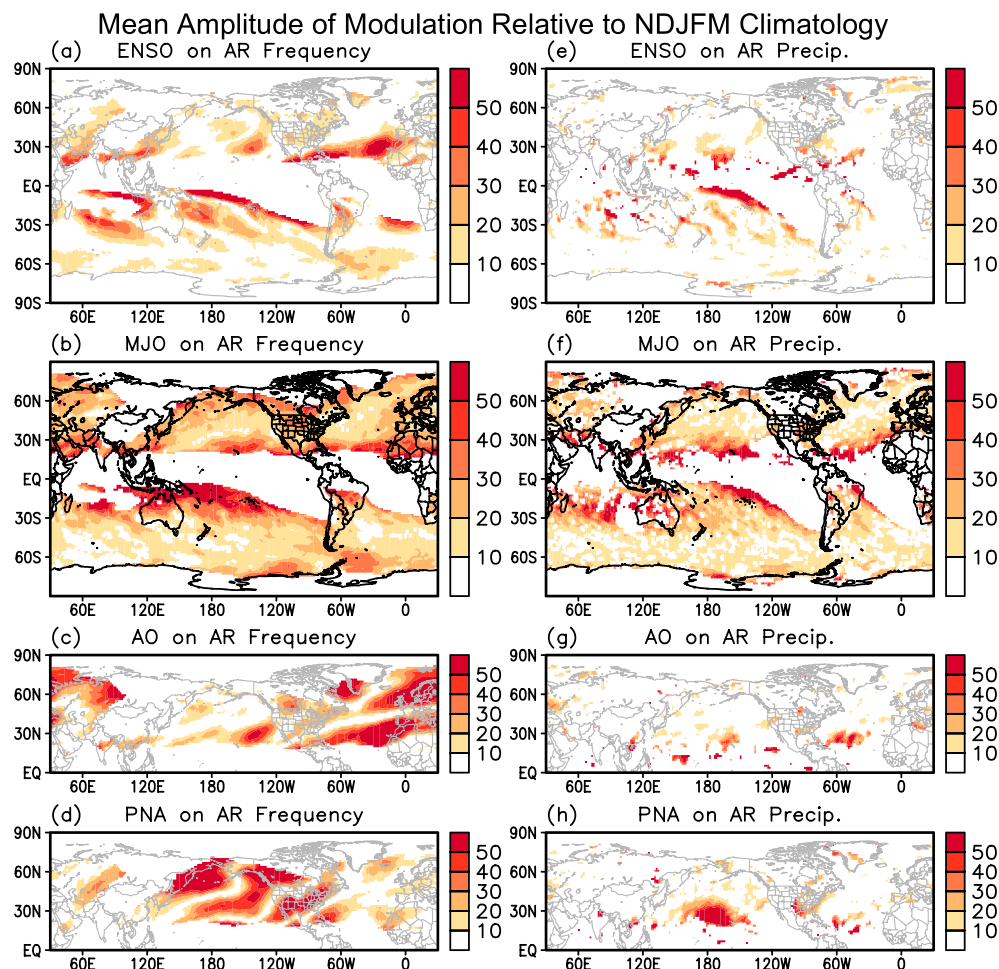


Figure 15. Mean amplitude of the modulation by ENSO, MJO, AO, and PNA on NDJFM AR frequency and precipitation scaled by the NDJFM climatology, shown in percentages. Mean amplitude is based on averaging the magnitude of modulation over the two phases of ENSO/AO/PNA or the eight phases of MJO as shown in Figures 10–14. Mean amplitude is calculated only if the anomalies are significant in at least one phase of the modes, and percentages relative to the climatology are shown only where the climatological AR frequency is over 2.5% or where the climatological AR precipitation is over 3 mm/d.

5. Conclusions

A technique is developed for objective detection of ARs on the global domain based on characteristics of IVT. The procedure involves the following three main steps: (1) extraction of the original set of objects (contiguous regions) where IVT is above the 85th percentile specific to each season and grid cell and a fixed lower limit of $100 \text{ kg m}^{-1} \text{ s}^{-1}$; (2) application of a set of criteria indicative of AR conditions with respect to IVT direction (coherent and directed along the shape elongation, with a mean poleward component $>50 \text{ kg m}^{-1} \text{ s}^{-1}$, length ($>2000 \text{ km}$), and length/width ratio (>2)) to these objects, resulting in a defined set of ARs; and (3) identification of landfall if the AR intersects the coastline, the mean AR IVT is directed from ocean to land, and the remaining length of the AR over the ocean is more than 1000 km. Among these steps, the strongest filtering (58% discarding rate) is associated with the geometry criteria (mostly the length limit), followed closely by the meridional IVT requirement (Table 1).

Output of the detection includes the AR shape, axis, landfall location (for landfalling ARs), and basic statistics of each detected AR (Figure 2). Overall, the procedure identified 281,616 ARs in the 18 year record (including the cases where a same AR system is detected multiple times at different time steps). On average 11 ARs are detected per IVT map, i.e., at any given time, for the globe. Out of these ARs, 24% are marked

as landfalls, which average to two to three landfalls at any given time. The ARs detected have a median length of ~ 3665 km, a median width of ~ 564 km, and a median length/width ratio of ~ 7 (Figures 6a–6c). AR IVT has a median of $\sim 374 \text{ kg m}^{-1} \text{ s}^{-1}$ and is predominantly directed northeastward in the Northern Hemisphere with a median azimuth of $\sim 56^\circ$ and southeastward in the Southern Hemisphere with a median azimuth of $\sim 121^\circ$ (Figures 6g and 6h).

Comparison to AR detection in the western North America, Britain, and East Antarctica with three independently conducted studies using different techniques shows over $\sim 90\%$ agreement in AR dates (Table 2). Sensitivity analysis suggests that among the parameters tested, AR detection has the largest sensitivity to the length criterion in terms of changes in the resulting statistical distribution of AR intensity and geometry (Figures 5a–5i). AR detection is more sensitive to the spatial resolution of the input data than the temporal resolution and the selection of a particular reanalysis product (Figures 5j–5l). Out of all ARs detected with ERA-Interim, 91% have a corresponding AR in MERRA within ± 6 h that overlaps by at least 50% area.

ARs occur more frequently in midlatitude ocean basins than over land and other latitudes, with centers of maximum frequency located in extratropical North Pacific/Atlantic, southeastern Pacific, and South Atlantic (Figure 7a). ARs account for 84% (88%) of the total meridional IVT and 8% (11%) of the zonal circumference between 30 and 50° in the Northern (Southern) Hemisphere (Figures 7b and 7c). Regions with more AR occurrences tend to have more persistent ARs as well (comparing Figures 7a and 7e). AR landfalls are most frequent along the west coasts of North America, southern South America, and Europe (Figure 8a). A notable number of AR landfalls occur in Greenland, Antarctica, and the Gulf of Mexico. Considerable AR landfalls also occur in regions where ARs have received less scientific attention, including South/East Asia, Australia and New Zealand, northeastern North America, central America/Caribbean, and northwestern/southwestern Africa.

The largest seasonal variations in AR frequency occur in the northeastern Pacific extending toward western U.S. and in southeastern Pacific extending to central Chile (Figures 9a and 9b). Considering the areas where ARs frequently make landfalls (see Figure 8a), the largest seasonal variations in AR precipitation occur along the west coast of North America (Figures 9d and 9e). The four large-scale climate modes examined, namely, ENSO, MJO, AO, and PNA, significantly modulate AR frequency and precipitation (with more localized patterns in the case of AR precipitation) during northern winters (Figures 10–14), with the magnitude of the modulation comparable to the amplitude of the seasonal cycle in various locations along the west coasts of North America and Europe (see Figure 9). The results are in broad consistency with previous studies that focused on the climate modulation of landfalling ARs along the west coasts of North America and Europe.

The global distribution of ARs and associated large-scale water vapor transport indicate a critical role for ARs in shaping the global water cycle. AR landfalls occur in all continents and major islands, which has implications to extreme meteorological/hydrological events and water resources in many locations. A catalog of global ARs identified in this study will be made available to the community for further analysis. Significant modulation of AR frequency and precipitation by large-scale climate modes suggests potential subseasonal to longer-term predictability of AR activities and their impacts given the time scales of these climate modes. The AR detection technique introduced herein will facilitate further investigations to understand how well the basic characteristics of ARs are represented in state-of-the-art weather/climate models and to assess the predictability and predictive skill of ARs in terms of AR occurrence, landfall, and impacts.

Acknowledgments

This research was supported by NSF AGS-1221013 and the NASA Energy and Water cycle Study (NEWS) program. The IWV-based AR landfall record was prepared and provided by Paul Neiman of the NOAA Earth System Research Laboratory and gratefully acknowledged. Comments and suggestions by Jinwon Kim of UCLA and Marty Ralph of UCSD/Scripps Institution of Oceanography were helpful and appreciated. This research was in part carried out on behalf of the Jet Propulsion Laboratory, California Institute of Technology, under a contract with the National Aeronautics and Space Administration.

References

- Backes, T. M., M. L. Kaplan, R. Schumer, and J. F. Mejia (2015), A climatology of the vertical structure of water vapor transport to the Sierra Nevada in cool season atmospheric river precipitation events, *J. Hydrometeorol.*, 16, 1029–1047, doi:10.1175/JHM-D-14-0077.1.
- Dee, D. P., et al. (2011), The ERA-Interim reanalysis: Configuration and performance of the data assimilation system, *Q. J. R. Meteorol. Soc.*, 137, 553–597, doi:10.1002/qj.828.
- Dettinger, M. (2011), Climate change, atmospheric rivers, and floods in California—A multimodel analysis of storm frequency and magnitude changes, *J. Am. Water Resour. Assoc.*, 47, 514–523, doi:10.1111/j.1752-1688.2011.00546.x.
- Dettinger, M. D. (2013), Atmospheric rivers as drought busters on the U.S. West Coast, *J. Hydrometeorol.*, 14, 1721–1732, doi:10.1175/JHM-D-13-02.1.
- Dettinger, M. D., F. M. Ralph, T. Das, P. J. Neiman, and D. R. Cayan (2011), Atmospheric rivers, floods, and the water resources of California, *Water*, 3, 445–478, doi:10.3390/w3020445.
- Gao, Y., J. Lu, L. R. Leung, Q. Yang, S. Hagos, and Y. Qian (2015), Dynamical and thermodynamical modulations on future changes of landfalling atmospheric rivers over western North America, *Geophys. Res. Lett.*, 42, 7179–7186, doi:10.1002/2015GL065435.
- Gimeno, L., R. Nieto, M. Vázquez, and D. A. Lavers (2014), Atmospheric rivers: A mini-review, *Front. Earth Sci.*, 2, 2.1–2.6, doi:10.3389/fearth.2014.00002.

- Gorodetskaya, I. V., M. Tsukernik, K. Claes, M. F. Ralph, W. D. Neff, and N. P. M. Van Lipzig (2014), The role of atmospheric rivers in anomalous snow accumulation in East Antarctica, *Geophys. Res. Lett.*, **41**, 6199–6206, doi:10.1002/2014GL060881.
- Guan, B., N. P. Molotch, D. E. Waliser, E. J. Fetzer, and P. J. Neiman (2010), Extreme snowfall events linked to atmospheric rivers and surface air temperature via satellite measurements, *Geophys. Res. Lett.*, **37**, L20401, doi:10.1029/2010GL044696.
- Guan, B., D. E. Waliser, N. P. Molotch, E. J. Fetzer, and P. J. Neiman (2012), Does the Madden-Julian Oscillation influence wintertime atmospheric rivers and snowpack in the Sierra Nevada?, *Mon. Weather Rev.*, **140**, 325–342, doi:10.1175/MWR-D-11-00087.1.
- Guan, B., N. P. Molotch, D. E. Waliser, E. J. Fetzer, and P. J. Neiman (2013), The 2010/2011 snow season in California's Sierra Nevada: Role of atmospheric rivers and modes of large-scale variability, *Water Resour. Res.*, **49**, 6731–6743, doi:10.1002/wrcr.20537.
- Hagos, S., L. R. Leung, Q. Yang, C. Zhao, and J. Lu (2015), Resolution and dynamical core dependence of atmospheric river frequency in global model simulations, *J. Clim.*, **28**, 2764–2776, doi:10.1175/JCLI-D-14-00567.1.
- Huffman, G. J., R. F. Adler, M. M. Morrissey, D. T. Bolvin, S. Curtis, R. Joyce, B. McGavock, and J. Susskind (2001), Global precipitation at one-degree daily resolution from multisatellite observations, *J. Hydrometeorol.*, **2**, 36–50, doi:10.1175/1525-7541(2001)002<0036:GPAODD>2.0.CO;2.
- Jeong, J.-H., and C.-H. Ho (2005), Changes in occurrence of cold surges over east Asia in association with Arctic Oscillation, *Geophys. Res. Lett.*, **32**, L14704, doi:10.1029/2005GL023024.
- Jiang, T., K. J. Evans, Y. Deng, and X. Dong (2014), Intermediate frequency atmospheric disturbances: A dynamical bridge connecting western U.S. extreme precipitation with East Asian cold surges, *J. Geophys. Res. Atmos.*, **119**, 3723–3735, doi:10.1002/2013JD021209.
- Lavers, D. A., and G. Villarini (2013a), Atmospheric rivers and flooding over the central United States, *J. Clim.*, **26**, 7829–7836, doi:10.1175/JCLI-D-13-00212.1.
- Lavers, D. A., and G. Villarini (2013b), The nexus between atmospheric rivers and extreme precipitation across Europe, *Geophys. Res. Lett.*, **40**, 3259–3264, doi:10.1002/grl.50636.
- Lavers, D. A., and G. Villarini (2015), The contribution of atmospheric rivers to precipitation in Europe and the United States, *J. Hydrol.*, **522**, 382–390, doi:10.1016/j.jhydrol.2014.12.010.
- Lavers, D. A., R. P. Allan, E. F. Wood, G. Villarini, D. J. Brayshaw, and A. J. Wade (2011), Winter floods in Britain are connected to atmospheric rivers, *Geophys. Res. Lett.*, **38**, L23803, doi:10.1029/2011GL049783.
- Lavers, D. A., G. Villarini, R. P. Allan, E. F. Wood, and A. J. Wade (2012), The detection of atmospheric rivers in atmospheric reanalyses and their links to British winter floods and the large-scale climatic circulation, *J. Geophys. Res.*, **117**, D20106, doi:10.1029/2012JD018027.
- Leung, L. R., and Y. Qian (2009), Atmospheric rivers induced heavy precipitation and flooding in the western U.S. simulated by the WRF regional climate model, *Geophys. Res. Lett.*, **36**, L03820, doi:10.1029/2008GL036445.
- Madden, R. A., and P. R. Julian (1971), Detection of a 40–50 day oscillation in the zonal wind in the tropical Pacific, *J. Atmos. Sci.*, **28**, 702–708, doi:10.1175/1520-0469(1971)028<0702:DOADOI>2.0.CO;2.
- Madden, R. A., and P. R. Julian (1972), Description of global-scale circulation cells in the tropics with a 40–50 day period, *J. Atmos. Sci.*, **29**, 1109–1123, doi:10.1175/1520-0469(1972)029<1109:DGSCC>2.0.CO;2.
- Matthews, A. J. (2000), Propagation mechanisms for the Madden-Julian Oscillation, *Q. J. R. Meteorol. Soc.*, **126**, 2637–2651, doi:10.1002/qj.49712656902.
- Moore, B. J., P. J. Neiman, F. M. Ralph, and F. E. Barthold (2012), Physical processes associated with heavy flooding rainfall in Nashville, Tennessee, and vicinity during 1–2 May 2010: The role of an atmospheric river and mesoscale convective systems, *Mon. Weather Rev.*, **140**, 358–378, doi:10.1175/MWR-D-11-00126.1.
- Nayak, M. A., G. Villarini, and D. A. Lavers (2014), On the skill of numerical weather prediction models to forecast atmospheric rivers over the central United States, *Geophys. Res. Lett.*, **41**, 4354–4362, doi:10.1002/2014GL060299.
- Neff, W., G. P. Compo, F. M. Ralph, and M. D. Shupe (2014), Continental heat anomalies and the extreme melting of the Greenland ice surface in 2012 and 1889, *J. Geophys. Res. Atmos.*, **119**, 6520–6536, doi:10.1002/2014JD021470.
- Neiman, P. J., F. M. Ralph, A. B. White, D. E. Kingsmill, and P. O. G. Persson (2002), The statistical relationship between upslope flow and rainfall in California's coastal mountains: Observations during CALJET, *Mon. Weather Rev.*, **130**, 1468–1492, doi:10.1175/1520-0493(2002)130<1468:TSRBUF>2.0.CO;2.
- Neiman, P. J., F. M. Ralph, G. A. Wick, J. D. Lundquist, and M. D. Dettinger (2008), Meteorological characteristics and overland precipitation impacts of atmospheric rivers affecting the West Coast of North America based on eight years of SSM/I satellite observations, *J. Hydrometeorol.*, **9**, 22–47, doi:10.1175/2007JHM855.1.
- Neiman, P. J., A. B. White, F. M. Ralph, D. J. Gottas, and S. I. Gutman (2009), A water vapor flux tool for precipitation forecasting, *Water Manage.*, **162**, 83–94, doi:10.1680/wama.2009.162.2.83.
- Neiman, P. J., L. J. Schick, F. M. Ralph, M. Hughes, and G. A. Wick (2011), Flooding in western Washington: The connection to atmospheric rivers, *J. Hydrometeorol.*, **12**, 1337–1358, doi:10.1175/2011JHM1358.1.
- Neiman, P. J., F. M. Ralph, B. J. Moore, M. Hughes, K. M. Mahoney, J. M. Cordeira, and M. D. Dettinger (2013), The landfall and inland penetration of a flood-producing atmospheric river in Arizona. Part I: Observed synoptic-scale, orographic, and hydrometeorological characteristics, *J. Hydrometeorol.*, **14**, 460–484, doi:10.1175/JHM-D-12-0101.1.
- Ralph, F. M., and M. D. Dettinger (2011), Storms, floods, and the science of atmospheric rivers, *Eos Trans. AGU*, **92**, 265, doi:10.1029/2011EO320001.
- Ralph, F. M., P. J. Neiman, and G. A. Wick (2004), Satellite and CALJET aircraft observations of atmospheric rivers over the eastern North Pacific Ocean during the winter of 1997/98, *Mon. Weather Rev.*, **132**, 1721–1745, doi:10.1175/1520-0493(2004)132<1721:SACAOO>2.0.CO;2.
- Ralph, F. M., P. J. Neiman, and R. Rotunno (2005), Dropsonde observations in low-level jets over the northeastern Pacific Ocean from CALJET-1998 and PACJET-2001: Mean vertical-profile and atmospheric-river characteristics, *Mon. Weather Rev.*, **133**, 889–910, doi:10.1175/MWR2896.1.
- Ralph, F. M., P. J. Neiman, G. A. Wick, S. I. Gutman, M. D. Dettinger, D. R. Cayan, and A. B. White (2006), Flooding on California's Russian River: Role of atmospheric rivers, *Geophys. Res. Lett.*, **33**, L13801, doi:10.1029/2006GL026689.
- Ralph, F. M., P. J. Neiman, G. N. Kiladis, K. Weickmann, and D. W. Reynolds (2011), A multi-scale observational case study of a Pacific atmospheric river exhibiting tropical-extratropical connections and a mesoscale frontal wave, *Mon. Weather Rev.*, **139**, 1169–1189, doi:10.1175/2010MWR3596.1.
- Ralph, F. M., G. A. Wick, P. J. Neiman, B. J. Moore, J. R. Spackman, M. Hughes, F. Yong, and T. Hock (2012), Atmospheric rivers in reanalysis products: A six-event comparison with aircraft observations of water vapor transport, Extended Abstracts, WCRP Reanalysis Conf., Silver Spring, 1 p., Md. [Available online at http://icr4.org/posters/Hughes_Atmospheric_Rivers.pdf.]
- Ralph, F. M., T. Coleman, P. J. Neiman, R. J. Zamora, and M. D. Dettinger (2013), Observed impacts of duration and seasonality of atmospheric-river landfalls on soil moisture and runoff in coastal northern California, *J. Hydrometeorol.*, **14**, 443–459, doi:10.1175/JHM-D-12-076.1.

- Ramos, A. M., R. M. Trigo, M. L. R. Liberato, and R. Tomé (2015), Daily precipitation extreme events in the Iberian Peninsula and its association with atmospheric rivers, *J. Hydrometeorol.*, **16**, 579–597, doi:10.1175/JHM-D-14-0103.1.
- Rienecker, M. M., et al. (2011), MERRA: NASA's Modern-Era Retrospective Analysis for Research and Applications, *J. Clim.*, **24**, 3624–3648, doi:10.1175/JCLI-D-11-00015.1.
- Rivera, E. R., F. Dominguez, and C. L. Castro (2014), Atmospheric rivers and cool season extreme precipitation events in the Verde River Basin of Arizona, *J. Hydrometeorol.*, **15**, 813–829, doi:10.1175/JHM-D-12-0189.1.
- Rutz, J. J., and W. J. Steenburgh (2012), Quantifying the role of atmospheric rivers in the interior western United States, *Atmos. Sci. Lett.*, **13**, 257–261, doi:10.1002/asl.392.
- Rutz, J. J., W. J. Steenburgh, and F. M. Ralph (2014), Climatological characteristics of atmospheric rivers and their inland penetration over the western United States, *Mon. Weather Rev.*, **142**, 905–921, doi:10.1175/MWR-D-13-00168.1.
- Rutz, J. J., W. J. Steenburgh, and F. M. Ralph (2015), The inland penetration of atmospheric rivers over western North America: A Lagrangian analysis, *Mon. Weather Rev.*, **143**, 1924–1944, doi:10.1175/MWR-D-14-00288.1.
- Stohl, A., C. Forster, and H. Sodemann (2008), Remote sources of water vapor forming precipitation on the Norwegian west coast at 60°N—A tale of hurricanes and an atmospheric river, *J. Geophys. Res.*, **113**, D05102, doi:10.1029/2007JD009006.
- Thompson, D. W. J., and J. M. Wallace (1998), The Arctic oscillation signature in the wintertime geopotential height and temperature fields, *Geophys. Res. Lett.*, **25**, 1297–1300, doi:10.1029/98GL00950.
- Trenberth, K. E. (1997), The definition of El Niño, *Bull. Am. Meteorol. Soc.*, **78**, 2771–2777, doi:10.1175/1520-0477(1997)078<2771:TDOENO>2.0.CO;2.
- Viale, M., and M. N. Nuñez (2011), Climatology of winter orographic precipitation over the subtropical central Andes and associated synoptic and regional characteristics, *J. Hydrometeorol.*, **12**, 481–507, doi:10.1175/2010JHM1284.1.
- Viale, M., R. A. Houze Jr., and K. L. Rasmussen (2013), Upstream orographic enhancement of a narrow cold-frontal rainband approaching the Andes, *Mon. Weather Rev.*, **141**, 1708–1730, doi:10.1175/MWR-D-12-00138.1.
- Waliser, D. E., et al. (2012), The "Year" of Tropical Convection (May 2008–April 2010): Climate variability and weather highlights, *Bull. Am. Meteorol. Soc.*, **93**, 1189–1218, doi:10.1175/2011BAMS3095.1.
- Wallace, J. M., and D. S. Gutzler (1981), Teleconnections in the geopotential height field during the Northern Hemisphere winter, *Mon. Weather Rev.*, **109**, 784–812, doi:10.1175/1520-0493(1981)109<0784:TITGHF>2.0.CO;2.
- Wheeler, M. C., and H. H. Hendon (2004), An all-season real-time multivariate MJO index: Development of an index for monitoring and prediction, *Mon. Weather Rev.*, **132**, 1917–1932, doi:10.1175/1520-0493(2004)132<1917:AARMMI>2.0.CO;2.
- Wheeler, M. C., H. H. Hendon, S. Cleland, H. Meinke, and A. Donald (2009), Impacts of the Madden–Julian Oscillation on Australian rainfall and circulation, *J. Clim.*, **22**, 1482–1498, doi:10.1175/2008JCLI2595.1.
- Wick, G., P. J. Neiman, and F. M. Ralph (2013), Description and validation of an automated objective technique for identification and characterization of the integrated water vapor signature of atmospheric rivers, *IEEE Trans. Geosci. Remote Sens.*, **51**, 2166–2176, doi:10.1109/TGRS.2012.2211024.
- Zhu, Y., and R. E. Newell (1998), A proposed algorithm for moisture fluxes from atmospheric rivers, *Mon. Weather Rev.*, **126**, 725–735, doi:10.1175/1520-0493(1998)126<0725:APAFMF>2.0.CO;2.